Recent recovery of Antarctic Bottom Water formation in the Ross Sea driven by climate anomalies

Alessandro Silvano, Annie Foppert, Stephen R. Rintoul, Paul R. Holland, Takeshi Tamura, Noriaki Kimura, Pasquale Castagno, Pierpaolo Falco, Giorgio Budillon, F. Alexander Haumann, Alberto C. Naveira Garabato, and Alison Macdonald

Publication date:

2020-11

Originally published in:

Nature Geoscience 13 (780–786), https://doi.org/10.1038/s41561-020-00655-3

Recent recovery of Antarctic Bottom Water formation in the Ross Sea driven by climate anomalies

Alessandro Silvano[1,2,3]*, Annie Foppert[2,3,4], Stephen R. Rintoul[2,3,4], Paul R. Holland[5], Takeshi Tamura[6,7], Noriaki Kimura[8], Pasquale Castagno[9], Pierpaolo Falco[9,10], Giorgio Budillon[9,10], F. Alexander Haumann[11,5], Alberto C. Naveira Garabato[1] and Alison Macdonald[12]

[1] Ocean and Earth Science, National Oceanography Centre, University of Southampton.
[2] CSIRO Oceans & Atmosphere, Hobart, Tasmania, Australia.
[3] Centre for Southern Hemisphere Oceans Research, Hobart, Tasmania, Australia
[4] Australian Antarctic Program Partnership, University of Tasmania, Hobart, TAS, Australia.
[5] British Antarctic Survey, Cambridge, United Kingdom
[6] National Institute of Polar Research, Tachikawa, Japan.
[7] SOKENDAI, Graduate University for Advanced Studies, Tachikawa, Japan.
[8] Atmosphere and Ocean Research Institute, The University of Tokyo, Tokyo, Japan
[9] Department of Sciences and Technologies, Parthenope University, Centro Direzionale, Isola C4, 80143 Napoli, Italy
[10] Consorzio Nazionale Interuniversitario per le Scienze del Mare, Roma, Italy
[11] Atmospheric and Oceanic Sciences, Princeton University, Princeton, NJ, USA.
[12] Woods Hole Oceanographic Institution, Woods Hole, MA, USA

*Corresponding author. A.Silvano@soton.ac.uk

Antarctic Bottom Water (AABW) supplies the lower limb of the global overturning circulation, ventilates the abyssal ocean, and sequesters heat and carbon on multidecadal to millennial timescales. AABW originates on the Antarctic continental shelf, where strong winter cooling and brine released during sea ice formation produces Dense Shelf Water that sinks to the deep ocean. The salinity, density and volume of AABW has decreased over the last 50 years, with the most dramatic changes observed in the Ross Sea. These changes have been attributed to increased melting of the Antarctic Ice Sheet. Here we use in situ observations to document a recovery in the salinity, density and thickness (i.e. depth range) of AABW formed in the Ross Sea, with properties in 2018-2019 similar to those observed in the 1990s. The recovery was caused by increased sea ice formation on the continental shelf. Increased sea ice formation was triggered by anomalous wind forcing associated with the unusual combination of positive Southern Annular Mode and extreme El Niño conditions between 2015 and 2018. Our study highlights the sensitivity of AABW formation to remote forcing and shows that climate anomalies can drive episodic increases in local sea ice formation that counter the tendency for increased ice sheet melt to reduce AABW formation.

Cold and dense AABW forms at the Antarctic margin and feeds the abyssal layer of the global ocean[1], supplying the lower limb of the global overturning circulation[2]. AABW occupies ~30-40% of the total volume of the global ocean[3] and is able to store heat and carbon in the abyss for several centuries[4]. Variability in AABW formation is thought to regulate atmospheric carbon dioxide concentrations, and therefore the Earth's climate, on centennial to millennial time scales[5,6].

Dense Shelf Water (DSW), the precursor for AABW, is produced on the Antarctic continental shelf where winter cooling and salinification by sea ice formation produces shelf waters of sufficient density to sink to the deep ocean. The strongest heat loss and salt injection occur in coastal polynyas, where persistent wind-driven export of sea ice allows continuous sea ice formation[7]. Once DSW escapes the continental shelf, it mixes with warmer ambient water (mostly Circumpolar Deep Water) to produce AABW. In recent decades AABW has freshened, decreased in density and its volume has contracted[8-11]. The most dramatic changes, especially in terms of freshening, have been observed in the Pacific and Indian sectors of the Southern Ocean[10], where AABW is primarily sourced from DSW from the continental shelf of the western Ross Sea[8,12,13].

Highly saline (absolute salinity>34.9 g kg^{-1}) DSW is found on the western Ross Sea continental shelf[14], where the high salinity is the result of both local and remote salt input to the ocean[15]. Local input comes from sea ice formation in the Terra Nova Bay Polynya, while remote input includes sea ice formation in the Ross Ice Shelf Polynya and on the broader continental shelf. Part of the salt input by these remote sources is advected toward Terra Nova Bay by coastal currents (Fig. 1a), contributing to the observed high salinity. Saline DSW leaves the western Ross Sea continental shelf near Cape Adare (Fig. 1a).

Salinification by sea ice formation is partially offset by freshwater entering from the Amundsen Sea[9]. This freshwater is advected toward the Ross Sea by westward flowing coastal currents. Enhanced ice-sheet melting into the Amundsen Sea is thought to have driven the observed freshening of DSW since the 1950s and, consequently, of AABW formed in the Ross Sea[9,16].

Here we show that the salinity, density and thickness of AABW increased in 2018 and 2019 downstream of the outflow from the western Ross Sea. We link this recovery to strong salinification of DSW from the western Ross Sea continental shelf observed between 2015 and 2018[17]. Finally, we show that increased DSW salinity is linked to anomalous interannual atmospheric forcing that has driven increased sea ice formation over the entire Ross Sea continental shelf. These atmospheric anomalies are associated with persistent positive Southern Annular Mode (SAM) and El-Niño conditions, highlighting the connection between remote forcing and AABW formation.

Recovery of AABW formed in the Ross Sea

Repeated summer hydrographic transects near Cape Adare (line S4P) and at 150°E are available between the early 1990s and 2018, along with some profiles collected at similar positions between 1969 and 1971, and in 2019 (see Methods and Fig. 1a). The AABW layer became fresher, lighter and thinner between the 1970s and the early 2010s (Fig. 1b-f). The most recent observations in 2018 and 2019 show a reversal of this pattern. At Cape Adare, just downstream of the main outflow of DSW from the western Ross Sea, the AABW layer in 2018 was 0.028±0.003 g kg^{-1} saltier (Fig. 1d), 0.028±0.008 kg m^{-3} denser (Fig. 1e) and 400±100 m thicker (Fig. 1f) than observed in 2011 (errors are one standard deviation of the observations). The densest water located near the sea floor, where the largest temporal differences were observed, was ~0.05 g kg^{-1} saltier in 2018 than in 2011 (Fig.1b). About 1000 km downstream at 150°E, the signal is damped (potentially due to mixing along the way), but the AABW layer was still 0.013±0.003 g kg^{-1} (~0.03 g kg^{-1} near the seafloor) saltier in 2019 than in 2011 (Figs. 1c and 1d). Here the 28.34 kg m^{-3} neutral density layer reappeared in 2018 after vanishing in the early 2010s (Fig. 1f). The AABW temperature did not show substantial changes (0.01±0.04°C at Cape Adare and 0.02±0.02°C at 150°E) between 2011 and 2018/19 (Figs. 1b and 1c), consistent with minimal changes in previous decades[9,18].

AABW formed in the Ross Sea freshened by about 0.01 g kg^{-1} per decade between the 1970s and the early 2010s[9,18]. The change in salinity between the 2011 and 2018 was both opposite in sign and about three times faster than observed before 2011 (or five times faster near the sea floor). Temporal changes in AABW could reflect changes in the volume transport and/or changes in the properties of DSW leaving the shelf. Temporal changes in the volume of DSW exported from the shelf can be driven by changes in the easterly winds at the shelf break of the western Ross Sea[19]. However, easterly winds did not exhibit anomalous changes between 2015 and 2018 in that region (Extended Data Fig. 1). Processes such as tides, mixing and eddies also influence cross-shelf exchange and AABW formation[20]. However, we do not expect these processes to drive interannual changes of AABW properties in the absence of interannual changes in wind or buoyancy forcing. In the absence of wind changes near the shelf break, we attribute the increase in AABW salinity, density and thickness to the rapid increase in salinity of DSW observed between 2015 and 2018 on the Ross Sea continental shelf[17] (see also Fig. 2a). Salinification of DSW acts to increase both the salinity and thickness of the newly formed AABW[18].

AABW recovery driven by increased sea ice production

Repeated summer measurements in Terra Nova Bay (see Fig. 1a for location) show a strong recovery in DSW salinity between 2015 and 2018[17] (see also Fig. 2a). An increase in salinity after 2015 was observed at three other sites on the western Ross Sea continental shelf[17]. Similarly, on the eastern continental shelf of the Ross Sea, cold (< -1.85°C) and deep (deepest ~ 200 m of the water column) waters became saltier after 2015 (Extended Data Fig. 2). Thus, in situ observations point to a salinification of dense waters after 2015 over the entire Ross Sea continental shelf.

Satellite-derived annual sea ice formation[21,22] integrated over the entire continental shelf increased strongly during the 2015-2018 period (Fig. 2a), consistent with the increase in salinity of DSW. Two complementary approaches (a sea ice concentration budget[23] and estimates of the net sea ice area exported out of the Ross Sea continental shelf[24-26], see Methods) provide confirmation of increased sea ice formation during this period. In this study we focus on interannual variability, as our time series are not long enough to investigate longer term (e.g. decadal) variability, and therefore time series are detrended for statistical analysis (see Methods, Extended Data Fig. 3, and, as an example, the dashed red line in Fig. 2a that shows the detrended DSW salinity time series in Terra Nova Bay). Correlation between sea ice formation and DSW salinity peaks at 1-year lag with sea ice formation leading (R ~0.65, 99% significant) and is relatively high (R > 0.4) for lags between 0 and 2 years (see Extended Data Fig. 3). Castagno et al.[17] show that an increase of ~65 km^3 $year^{-1}$ in sea ice formation is required to account for DSW salinity changes (0.02-0.03 g kg^{-1} $year^{-1}$) between 2015 and 2018. The observed increase in sea ice formation (~100-150 km^3 $year^{-1}$; see Extended Data Fig. 3b) is sufficient to accomplish the salinity changes, considering that not all released salt accumulates in DSW. Correlations between DSW salinity and sea ice formation in the

Ross or Terra Nova Bay polynyas are lower (Extended Data Fig. 3), indicating that DSW properties in Terra Nova Bay are influenced by sea ice formation over the broader continental shelf.

Changes in other freshwater sources are unlikely to explain the rapid increase in DSW salinity observed during the 2015-2018 period (see "Freshwater sources to the Ross Sea continental shelf" in the Methods). In particular, hydrographic observations on the eastern Ross Sea continental shelf do not show a reduction in freshwater import from the Amundsen Sea in recent years[27], and ice sheet discharge into the Amundsen Sea has continued to rise during the last decade[28], indicating that changes in glacial meltwater transported by coastal currents from the Amundsen Sea cannot explain the increase in DSW salinity in the Ross Sea. In conclusion, our analysis indicates that sea ice formation over the Ross Sea continental shelf is the dominant factor in driving interannual changes in DSW salinity in Terra Nova Bay. DSW salinity lags sea ice formation by about one year. These results link the recent increase in DSW salinity and the associated recovery in AABW formation to an increase in sea ice formation over the Ross Sea continental shelf (Figs. 2a and 3b). We now discuss the drivers of increased sea ice formation between 2015 and 2018.

Increased sea ice formation driven by reduced sea ice import

Near the Antarctic coast, sea ice flows westward from the Amundsen Sea toward the Ross Sea driven by easterly winds (Figs. 4c and Extended Data Fig. 4). We link increased sea ice formation between 2015 and 2018 over the Ross Sea continental shelf to a reduction in the inflow of sea ice from the Amundsen Sea (Fig. 2b). Indeed, sea ice formation and inflow are strongly negatively correlated ($R=-0.65$; significant at 99%). Reduced sea ice import during summer (November to February) resulted in lower sea ice concentration over the Ross Sea continental shelf at the end of summer (i.e. February, Fig. 3d), conditions favourable to enhanced sea ice formation in early winter (March to May; Extended Data Fig. 5). Sea ice concentration in February preconditions sea ice formation in the following early winter, whereby less sea ice allows enhanced growth in open waters when air temperature drops at the beginning of the winter season[29]. Reduced sea ice import during winter (March to October; Extended Data Fig. 5) was associated with a reduction in sea ice concentration in the southern Ross Sea over the same period (Fig. 3f). Lower sea ice concentration enhances sea ice formation in leads and reduces mechanical stresses and associated sea ice rafting and ridging[23]. Smaller mechanical stress allowed greater sea ice divergence and an increase in the size and activity (i.e. sea ice formation) of the Ross Ice Shelf Polynya (Fig. 3b). Thus, more open water, increased sea ice divergence, and a larger and more active Ross Ice Shelf Polynya acted together to increase sea ice formation over the continental shelf throughout the winter (Figs. 2 and 3b). A sea ice concentration budget[23] (see Methods) confirms increased sea ice formation concurrent with increased sea ice divergence and reduced sea ice rafting and ridging between 2015 and 2018 on the Ross Sea continental shelf.

Processes other than a decrease in sea ice import can potentially cause a reduction in sea ice concentration over the Ross Sea continental shelf, including increased southerly winds pushing sea ice offshore or enhanced local sea ice melting in summer. However, between 2015 and 2018, there were neither anomalous southerly winds nor anomalous local sea ice melting (see Methods and Extended Data Fig. 6). Thus, our statistical and mechanistic analyses point to the decrease of sea ice inflow from the Amundsen Sea as the key driver of increased sea ice formation over the Ross Sea continental shelf between 2015 and 2018. We next show how climate forcing caused the reduction in sea ice import into the Ross Sea.

Reduced sea ice import driven by climate anomalies

Reduced sea ice inflow from the Amundsen Sea between 2015 and 2018 resulted from a combination of weakened easterly winds and anomalously low sea ice concentration in the western Amundsen Sea (Figs. 4a and 4b). This combination is particularly apparent in summer, when sea ice concentration was strongly diminished and the strength of the easterly winds steadily declined. Summer easterly winds and sea ice concentration in the western Amundsen Sea are strongly correlated (0.73, significant at 99%), suggesting that reduced import of sea ice from the eastern Amundsen Sea, driven by reduced easterly winds, was the main driver of the reduced sea ice concentration in the west between 2015 and 2018. During winter in the years 2015 to 2018, sea-ice concentrations were also low, while easterly winds did not show a sustained decline as observed in summer. We argue that the low sea ice concentration during winter was preconditioned by summer conditions, consistent with previous work[30] showing that reduced summer sea ice increases upper ocean heat content by solar radiation, reducing winter sea ice. This mechanism is supported by the strong correlation (R=0.63, significant at 99%) we find between summer and winter sea ice concentration in the western Amundsen Sea. Thus, our analysis suggests that reduced summertime easterly winds drove year-round reduction in sea ice concentration in the western Amundsen Sea and reduced sea ice inflow into the Ross Sea. We now conclude our analysis by linking reduced summer easterly winds with climatic forcing.

Two climate indices represent the dominant modes of atmospheric variability in the Pacific sector of the Southern Ocean: SAM and the Southern Oscillation Index (SOI)[31]. SAM, to first order, describes the strength of the westerly winds and is associated with pressure anomalies over the entire Southern Ocean. SOI captures variability associated with the El Niño/La Niña cycle, which affects the low-pressure system over the Amundsen Sea (Amundsen Sea Low). Anomalous positive SAM (westerly anomalies) and negative SOI (El Niño, weakened Amundsen Sea Low) occurred between 2015 and 2018. This superposition is rare as the two indices are generally in phase[31]. Positive SAM and negative SOI anomalies occurred together in summer 2015, 2016 and, to lesser extent, in 2018 (Fig. 5a). In winter, this combination emerged clearly only in 2015 (Extended Data Fig. 7), consistent with the hypothesis that summer winds dominated the ocean-sea ice response. A multiple regression analysis (see Methods) confirms that positive SAM is associated with low pressures causing westerly anomalies that extend to the Antarctic coast (Fig. 5c). Negative SOI weakens the Amundsen Sea Low, generating an anticyclonic anomaly in the Amundsen Sea and westerly anomalies near the coast (Fig. 5d). The combination of positive SAM and negative SOI weakened summer easterlies in the western Amundsen Sea (Fig. 5b), ultimately leading to the recent recovery of AABW formed in the Ross Sea.

Response of AABW formation to climate anomalies

Observations during the past half century have shown sustained freshening, decrease in density and contraction of AABW formed in the Ross Sea[8-10]. Counter to this multi-decadal tendency, recent observations reveal a sharp increase in salinity, density and thickness of AABW, with properties in 2018-2019 comparable to those observed in the 1990s. Observations in the abyssal Southern Ocean are sparse and we therefore cannot rule out similar rapid changes in the past. However, the magnitude and speed of the recent changes (five times faster than changes observed in previous decades near the sea floor) suggest that the recent recovery is associated with an unusual climate anomaly. Here, we have outlined a five-step process by which large-scale climate perturbations were transferred to the abyssal Southern Ocean (Fig. 6). 1) The rare combination of positive SAM and negative SOI (El-Niño) between 2015 and 2018 triggered a weakening of the easterly winds in the Amundsen Sea. 2) Weakened easterlies caused a reduction of sea ice import from the Amundsen into the Ross Sea. 3) Reduced sea ice import drove increased sea ice formation over the Ross Sea continental shelf by making sea ice more dynamic (i.e. lower sea ice concentration, less ridging and rafting, more divergence). 4) Increased sea ice formation enhanced the salinity of DSW formed on the Ross Sea continental shelf. 5) Finally, enhanced salinity of DSW escaping the continental shelf of the western Ross Sea drove an increase in the salinity, density and thickness of AABW. These results highlight the sensitivity of AABW formation to forcing from climate phenomena associated with dynamics of the tropics (El Niño) and the upper atmosphere (SAM). The unusual combination of positive SAM and El Niño between 2015-2018 produced anomalies in surface winds and, in turn, sea ice formation of sufficient magnitude to compensate for two decades of freshening at the long-term mean rate observed prior to 2015.

Interannual changes in sea ice formation and hence AABW properties in the Weddell Sea have also been attributed to wind anomalies associated with climate modes[32,33], although lack of observations on the continental shelf prevents an assessment of the link between winds and AABW formation there[34]. There is now evidence that the abyssal Southern Ocean can rapidly respond to climatic forcing. Future climate projections under sustained anthropogenic forcing show that positive SAM anomalies will become more common[35,36], along with the frequency of extreme El-Niño events[37] (as observed in 2015-2016). It is also projected that the El Niño-negative SAM relationship observed during the past decades will weaken in a warming climate[38]. The combination of these projected changes may lead to more frequent occurrences of simultaneous El Niño and positive SAM anomalies (as observed during the 2015-2018 period), possibly enhancing AABW formation.

Climate models predict that AABW formation will reduce in a warming climate as a result of increased freshwater input by the Antarctic Ice Sheet[39], and there is some evidence that this is already happening[9,40]. However, at present, climate models do not well reproduce the complex interactions between the ocean, sea ice, ice sheet and atmosphere in Antarctica[41], and therefore they cannot capture the physical mechanisms shown here to drive the recent renewal in AABW formation. Our study establishes that climate anomalies can lead to episodes of enhanced sea ice formation that counter the impact of ice sheet melting, causing enhanced AABW formation. The interplay between these processes needs to be resolved if we aim to assess how climate change will affect the abyssal ocean and its ability to store heat and carbon in decades and centuries to come.

References

1. Orsi, A. H., Johnson, G. C. & Bullister, J. L. Circulation, mixing, and production of Antarctic Bottom Water. *Prog. Oceanogr.* **43**, 55–109 (1999).
2. Lumpkin, R. & Speer, K. Global ocean meridional overturning. *J. Phys. Oceanogr*. **37**, 2550–2562 (2007).
3. Johnson, G. C. Quantifying Antarctic Bottom Water and North Atlantic Deep Water volumes. *J. Geophys. Res.* **113**, C05027 (2008).
4. de Lavergne, C., Madec, G., Roquet, F., Holmes, R. & McDougall, T. Abyssal ocean overturning shaped by seafloor distribution. *Nature* **551**, 181 (2017).
5. Sigman, D. M. & Boyle, E. A. Glacial/interglacial variations in atmospheric carbon dioxide. *Nature* **407**, 859–869 (2000).
6. Ferrari, R. *et al.* Antarctic sea ice control on ocean circulation in present and glacial climates. *Proc. Nat /Acad. Sci*. **111,** 8753–8758 (2014).
7. Nihashi, S. & Ohshima, K. I. Circumpolar mapping of antarctic coastal polynyas and landfast sea ice: relationship and variability. *J Clim.* **28**, 3650–3670 (2015).
8. Rintoul, S. R. Rapid freshening of Antarctic Bottom Water formed in the Indian and Pacific oceans. *Geophys. Res. Lett.* **34**, L06606 (2007).
9. Jacobs, S. S. & Giulivi, C. F. Large multidecadal salinity trends near the Pacific-Antarctic continental margin. *J. Clim.* **23**, 4508–4524 (2010).
10. Purkey, S. G. & Johnson, G. C. Antarctic bottom water warming and freshening: contributions to sea level rise, ocean freshwater budgets, and global heat gain. *J. Clim.* **26**, 6105–6122 (2013).
11. Menezes, V. V., Macdonald, A. M. & Schatzman, C. Accelerated freshening of Antarctic Bottom Water over the last decade in the Southern Indian Ocean. *Sci. Adv.* **3**, 1–10 (2017).
12. Gordon, A. L., Orsi, A., Muench, R. & Visbeck, M. Western Ross Sea continental slope gravity currents. *Deep Sea Res. II* **56**, 796–817 (2009).
13. Shimada, K., Aoki, S., Ohshima, K. I. & Rintoul S. R. Influence of Ross Sea Bottom Water changes on the warming and freshening of the Antarctic Bottom Water in the Australian-Antarctic basin. *Ocean Sci.* **8**, 419–432 (2012).
14. Orsi, A. H. & Wiederwohl, C. L. A recount of Ross Sea waters. *Deep Sea Res. Part II Top.*

Stud. Oceanogr. **56**, 778–795 (2009).

15. Jendersie, S., Williams, M. J., Langhorne, P. J. & Robertson, R. The density-driven winter intensification of the Ross Sea circulation. *J. Geophys. Res. Oceans* **123**, 7702– 7724 (2018).
16. Nakayama, Y., Timmermann, R., Rodehacke, C. B., Schröder, M. & Hellmer, H. H. Modeling the spreading of glacial meltwater from the Amundsen and Bellingshausen Seas. *Geophys. Res. Lett.* **41**, 7942–7949 (2014).
17. Castagno, P., *et al.* Rebound of shelf water salinity in the Ross Sea. *Nat. Commun.* **10,** 5441 (2019).
18. van Wijk, E. M. & Rintoul, S. R. Freshening drives contraction of Antarctic Bottom Water in the Australian Antarctic Basin. *Geophys. Res. Lett.* **41**, 1657–1664 (2014).
19. Gordon, A. L., Huber, B. A., & Busecke, J. Bottom water export from the western Ross Sea, 2007 through 2010. *Geophys Res Lett.* **42**, 5387–5394 (2015).
20. Budillon, G., Castagno, P., Aliani, S., Spezie, G. & Padman, L. Thermohaline variability and Antarctic bottom water formation at the Ross Sea shelf break. *Deep. Res. Part I Oceanogr. Res. Pap.* **58**, 1002–1018 (2011).
21. Tamura, T., Ohshima, K. I., Nihashi, S. & Hasumi, H. Estimation of surface heat/salt fluxes associated with sea ice growth/melt in the southern ocean. *SOLA* **7**, 17–20 (2011).
22. Tamura, T., Ohshima, K. I., Fraser, A. D. & Williams, G. D. Sea ice production variability in Antarctic coastal polynyas. *J. Geophys. Res.* **121**, 2967–2979 (2016).
23. Holland, P. R. & Kimura, N. Observed concentration budgets of Arctic and Antarctic sea ice. *J. Clim.* **29**, 5241–5249 (2016).
24. Comiso, J. C., Kwok, R., Martin, S. & Gordon, A. L. Variability and trends in sea ice extent and ice production in the Ross Sea. *J. Geophys. Res.* **116**, C04021 (2011).
25. Drucker, R., Martin, S. & Kwok, R. Sea ice production and export from coastal polynyas in the Weddell and Ross Seas. *Geophys. Res. Lett.* **38**, L17502 (2011).
26. Kwok, R., Pang, S. S. & Kacimi, S. Sea ice drift in the Southern Ocean: regional patterns, variability, and trends. *Elem. Sci. Anth*. **5** (2017).
27. Porter, D. F. *et al.* Evolution of the seasonal surface mixed layer of the Ross Sea, Antarctica, observed with autonomous profiling floats. *J. Geophys. Res. Ocean.* **124**, 4934–4953 (2019).
28. Rignot, E. *et al.* Four decades of Antarctic Ice Sheet mass balance from 1979–2017. *Proc. Natl Acad. Sci.* **116**, 1095–1103 (2019).
29. Nicholls, K. W. & Østerhus, S. Interannual variability and ventilation timescales in the

ocean cavity beneath Filchner-Ronne Ice Shelf, Antarctica. *J. Geophys. Res.* **109**, C04014 (2004).

30. Holland, P. R. The seasonality of Antarctic sea ice trends. *Geophys. Res. Lett.* **41**, 4230–4237 (2014).
31. Fogt, R. L., Bromwich, D. H. & Hines, K. M. Understanding the SAM infuence on the South Pacific ENSO teleconnection. *Clim. Dyn.* **36**, 1555–1576 (2011).
32. Gordon, A. L., Huber, B., McKee, D. & Visbeck, M. A seasonal cycle in the export of bottom water from the Weddell Sea. *Nature Geosci.* **3,** 551–556 (2010).
33. McKee, D. C., Yuan, X., Gordon, A. L., Huber, B. A. & Dong, Z. Climate impact on interannual variability of Weddell Sea Bottom Water. *J. Geophys. Res.* **116**, C05020 (2011).
34. Abrahamsen, E. P., *et al.* Stabilization of dense Antarctic water supply to the Atlantic Ocean overturning circulation. *Nat. Clim. Chang.* **9,** 742–746 (2019).
35. Fyfe, J. C., Saenko, O. A., Zickfeld, K., Eby, M. & Weaver, A. J. The role of poleward-intensifying winds on southern ocean warming. *J. Clim.* **20**, 5391–5400 (2007).
36. Sigmond, M., Reader, M. C., Fyfe, J. C. & Gillett, N. P. Drivers of past and future Southern Ocean change: Stratospheric ozone verses greenhouse gas impact. *Geophys. Res. Lett.* **38**, L12601 (2011).
37. Cai, W. et al. Increasing frequency of extreme El Niño events due to greenhouse warming. *Nat. Clim. Change* **4**, 111–116 (2014).
38. Lim, E., *et al.* Continuation of tropical Pacific Ocean temperature trend may weaken extreme El Niño and its linkage to the Southern Annular Mode. *Sci. Rep.* **9,** 17044 (2019).
39. Lago, V. & England, M. H. Projected slowdown of Antarctic Bottom Water formation in response to amplified meltwater contributions. *J Clim.* **32**(19), 6319-6335 (2019).
40. Silvano, A. et al. Freshening by glacial meltwater enhances melting of ice shelves and reduces formation of Antarctic Bottom Water. *Sci. Adv.* **4**, eaap9467 (2018).
41. Heuzé, C., Heywood, K. J., Stevens, D. P. & Ridley, J. K. Southern Ocean bottom water characteristics in CMIP5 models. *Geophys. Res. Lett.* **40,** 1409–1414 (2013).
42. Arndt, J. E. et al. The International Bathymetric Chart of the Southern Ocean (IBCSO) Version 1.0-A new bathymetric compilation covering circum-Antarctic waters. *Geophys. Res. Lett.* **40**, 3111–3117 (2013).

Acknowledgments

This research was supported by the Centre for Southern Hemisphere Oceans Research (CSHOR), a partnership between the Commonwealth Scientific and Industrial Research Organisation (CSIRO) and the Qingdao National Laboratory for Marine Science, as well as the Antarctic Climate and Ecosystems Cooperative Research Centre, the Australian Antarctic Program Partnership and the Earth Systems and Climate Change Hub of the Australian Government's National Environmental Science Program. A.S., P.H, and A.C.N.G. acknowledges funding from NERC (grant number NE/SO11994/1). F.A.H. was supported by the SNSF grant numbers P2EZP2_175162 and P400P2_186681 and NSF grant number PLR-1425989.

Author contributions

A.S. and S.R.R. coinceved the study. A.S., A.F. and S.R.R. analysed the oceanographic data. S.R.R., P.C., P.F., G.B. and A.M. collected part of the oceanographic data used in this study. A.S., P.R.H., T.T. and N.K. analysed the sea ice and atmospheric data. F.A.H. and A.C.N.G. provided essential insight in the interpretation of the observations. A.S. wrote the manuscript with input from all the co-authors.

Competing interests

The authors declare no competing interests.

Fig. 1| Recovery of AABW formed in the Ross Sea. a, Map of the study area with bathymetry overlaid[42]. Crosses indicate observations from the Eltanin expedition in 1969-1971, while orange dots denote data collected by a deep float in 2019 (see Methods). **b**, **c**, Conservative temperature (°C) versus absolute salinity (g kg^{-1}) at Cape Adare and at 150°E (see location in **a**). Overlaid are the 28.30, 28.32 and 28.34 kg m^{-3} neutral density surfaces for reference. **d**, **e**, Average AABW absolute salinity and neutral density. AABW is defined[18] as water denser than 28.30 kg m^{-3}. **f**, Thickness of the 28.30 (dashed black) and 28.34 (solid black) kg m^{-3} layers at Cape Adare and thickness of the 28.34 kg m^{-3} layer at 150°E (red). Thickness is calculated between the depth of the density surface and the sea floor. Mean (dots) and standard deviation (vertical bars) are calculated using observations collected each year along the two transects. Observations from the Eltanin expedition are temporally averaged between 1969 and 1971.

Fig. 2| Link between DSW salinity, sea ice production and import. a, DSW salinity (g kg^{-1}, solid red) measured near the sea floor in Terra Nova Bay[17] (see Methods) and yearly (March to October) sea ice production (km^3, solid black) over the Ross Sea continental shelf between 1992 and 2018. Note that some years are missing in the DSW salinity time series. The dashed red line is the detrended DSW salinity. **b**, Yearly (November to October) sea ice area (10^5 km^2) imported from the Amundsen Sea into the Ross Sea (blue), calculated across the gate shown in Fig. 4c (see Methods). Note that the y-axis is reversed. Overlaid is the yearly sea ice production as in **a**.

Fig. 3 | Sea ice changes in the Ross Sea. a, Climatological yearly (March to October) sea ice production (m) over the Ross Sea continental shelf. **b**, Anomaly of sea ice production temporally averaged between 2015 and 2018. In **a** and **b** the 5-m yearly sea ice production contour is in solid black to capture the edge of coastal polynyas, while the 0.5-m contour in dashed black highlights areas outside coastal polynyas with relatively high rates of sea ice production. **c**, Climatological sea ice concentration (%) in February over the southern Ross Sea. **d**, Anomaly of February sea ice concentration temporally averaged between 2015 and 2018. **e**, **f** Same as **c**, **d** but for winter (March to October). Climatologies and anomalies are defined in the Methods.

Fig. 4| Interannual variability of winds and sea ice in the western Amundsen Sea. a, Summer (November to February) anomalies of easterly winds (m s^{-1}) and sea ice concentration (%) in the western Amundsen Sea between 1992 and 2018 (see Methods). Values are obtained from a spatial average inside the black box in **c**. The south-north transect on the western side of the box represents the gate used to estimate the sea ice inflow from the Amundsen to the Ross Sea. Easterly winds are obtained by rotating the coordinate system counterclockwise by 30° to follow the coastline. **b**, Same as **a** for winter (March to October). **c** (**d**) Summer climatology (2015-2018 anomaly) of winds (vectors) and sea ice concentration (background color) in the Ross and western Amundsen seas.

Fig. 5 | Anomalous climate forcing between 2015 and 2018. a, Summer anomalies of SAM (black) and SOI (red) between 1992 and 2018. The 2015-2018 period is characterized by positive SAM and negative SOI. **b**, Multiple regression (see Methods) of SAM and SOI onto mean sea level pressure (mbar, red lines), and associated winds (m s^{-1}, black vectors). Contours of mean sea level pressure are every 0.5 mbar. Solid (dashed) lines mean positive (negative) anomalies. **c**, SAM component of the regression. This panel highlights atmospheric variability associated with positive SAM. **d**, Same as **c**, for (negative) SOI. In this panel contours are every 0.25 mbar. Note how both positive SAM and negative SOI cause westerly anomalies over the Amundsen Sea.

Fig 6| Schematic illustrating the physical mechanisms driving enhanced AABW formation in the Ross Sea. The unusual combination of positive SAM and El-Niño resulted in weaker easterly winds in the western Amunsen Sea, less import of sea ice, and a more open sea ice pack with higher rates of sea ice formation on the Ross Sea continental shelf. The resulting increase in DSW salinity enhanced the formation of AABW.

Methods

Datasets

The data used in the study are summarised below.

1) Oceanography Data

Repeat hydrographic sections were occupied along the S4P line and at 150°E (P11S) between the early 1990s and 2018 (Fig. 1a). Data were collected and made publicly available by the International Global Ship-based Hydrographic Investigations Program (GO-SHIP; http://www.go-ship.org/) and the national programs that contribute to it. Profiles were collected between January and March (except for an April cruise in 1993 at 150°E) to minimize aliasing due to seasonal variability. Temperature, practical salinity and pressure measurements are accurate to within ±0.002°C, ±0.002 psu, and ±3 dbar, respectively. We also use summer CTD profiles[43] (https://www.nodc.noaa.gov) from a series of cruises conducted onboard RV Eltanin between 1969 and 1972 located near the repeat sections[8,18]. The accuracy of the Eltanin observations was not reported, but accuracies in other oceanographic cruises during the same period are likely to be indicative: ±0.005°C for temperature, ±0.003 to 0.01 in salinity, and ±0.5% for pressure[44]. Finally, we use data collected by a deep Argo float (WMO: 7900635, http://www.argodatamgt.org; deployed on 2 February 2019 near 151.5°E, 65°S). Profiles were collected between February and early April 2019 nearby the 150°E section (see Fig. 1a). Capable of withstanding pressures as high as 6000 dbar[45], the float profiles from the sea surface to seafloor. The salinity profiles were calibrated post-deployment against a nearby shipboard CTD cast taken the previous year at 150°E, 64.6°S on the R/V Investigator voyage IN2018_V01. Calibrations were done in T-S space and within the stable part of the water column, i.e. between 2000 dbar and the deep salinity minimum, such that an anomalous linear freshening with pressure is removed. After the correction to salinity has been made, the mean (median) offset between the float and shipboard salinities is 0.00025 psu (0.00021 psu).

All these observations are used here to investigate temporal changes in AABW properties.

Practical salinity and potential temperature are converted into absolute salinity (g kg^{-1}) and conservative temperature (°C), respectively, while Neutral Density (kg m^{-3}) is used to characterize water density[46].

Hydrographic measurements in Terra Nova Bay (74.75°S–75.50°S, 163°E–166°E) have been collected as part of the long term (1995 to present) Italian National Antarctic Research Programme (PNRA; http://morsea.uniparthenope.it). We also use measurements collected during two Nathaniel B. Palmer expeditions in 2013 and 2018 as part of the TRACERS (https://doi.org/10.1594/IEDA/320068) and CICLOPS (https://www.bco-dmo.org/dataset/783911) projects, respectively. DSW properties are measured in the core of the Drygalski Trough (bottom depth > 800 m) between 870 and 900 m depth, where the densest water accumulates. The reader is referred to Castagno et al.[17] for more details about this dataset. Measurements have been mostly collected toward the end of the austral summer season (around February). Since summer DSW properties are influenced by sea ice formation during previous winter(s), the DSW salinity time series is shifted back by one year to investigate its co-variability with sea ice formation.

We use data collected by two APEX profiling floats (WMO: 5904150, 5904152; http://www.argo.ucsd.edu) deployed in December 2013 from the U.S. icebreaker Nathaniel B. Palmer, cruise NPB-1310, on the eastern Ross Sea continental shelf (see Extended Data Fig. 2 for location). Float 5904150 collected data on the eastern Ross Sea continental shelf for about 3 years before drifting away, while float 5904152 sampled that area for about 4 years. The reader is referred to Porter et al.[27] for more details about measurements collected by these floats.

2) Atmospheric Reanalysis

We use daily atmospheric data provided by the ERA5 re-analysis[47] (https://www.ecmwf.int/en/forecasts/datasets/reanalysis-datasets/era5). More specifically, we use surface winds at 10 m height, mean sea level pressure and surface air temperature.

3) Sea Ice Data

SEA ICE CONCENTRATION: We use two satellite-derived daily products for sea ice concentration. The first product is version 3 of NOAA/NSIDC Climate Data Record of Passive Microwave Sea Ice Concentration[48] (CDR; https://nsidc.org/data/G02202/versions/3). Here, we use data from November 1991 to December 2018. The second product is the AMSR-E/AMSR2[49] (advanced microwave scanning radiometer; https://nsidc.org/data/AU_SI12/versions/1). We use data from 2003 to 2010 (AMSR-E) and from 2013 to 2018 (AMSR2).

SEA ICE MOTION: We use three different daily products for sea ice motion that, for simplicity, we name 1) "Pathfinder", 2) "Kimura" and 3) "wind approximation". 1) The first product is the Polar Pathfinder[50] (https://nsidc.org/data/NSIDC-0116/versions/4), covering the period between November 1991 and December 2018 (for our study). 2) We also derive ice drift using a cross-correlation technique applied to AMSR-E/AMSR2 brightness temperatures[23], providing year-round data between 2003 and 2010 and between 2013 and 2018. We use the Kimura dataset, along with AMSR-E/AMSR2 sea ice concentration, to calculate the sea ice budget. 3) Finally, we approximate sea ice motion using surface winds. Sea ice speed is taken to be 2% of the surface wind speed, while sea ice is assumed to drift in the same direction of the surface winds as the turning angle of sea ice relative to the wind is small[51,52] (0 to 15° to the left of the wind direction). Results are not sensitive to the parameters chosen for the wind approximation, meaning that the levels of significance of the correlations shown in this study do not change if the scaling factor is varied by ±1% or the turning angle by 15°. We use ERA5 to infer sea ice motion because it provides year-round and long-term (i.e. several decades) data, while other datasets are either too short (Kimura) or do not well reproduce sea ice motion in summer[24] (Pathfinder). The "wind approximation", along with CDR sea ice concentration, is used to estimate interannual variability of sea ice imported from the Amundsen Sea into the Ross Sea. The ERA5-based estimate is consistent with estimates from the other two datasets (Pathfinder and Kimura) during winter (see Extended Data Fig. 4d), confirming that winds can be used to approximate sea ice flow, at least in the area we are interested in. In other regions this approximation works less well, as for example near Cape

Adare where most of the sea ice is exported out of the Ross Sea continental shelf (Extended Data Fig. 4). Here the wind approximation overestimates the export (Extended Data Fig. 4e), presumably due to strong sea ice ridging occurring there (see sea ice concentration budget) that cannot be captured by this approximation. As such, the sea ice export through a transect that encloses the Ross Sea continental shelf, as done for winter months in previous studies[24-26], cannot be properly estimated using the wind approximation.

SEA ICE FORMATION: Monthly sea ice production is derived from satellite microwave measurements brightness temperature data (Defense Meteorological Satellite Program (DMSP) Special Sensor Microwave Imager, SSM/I; https://nsidc.org/data/smmr_ssmi) following Tamura et al.[21,22]. The method allows estimation of sea ice formation in areas of thin (< 0.2 m) sea ice. In this calculation, sea ice formation is assumed to be zero where sea ice is thick (> 0.2 m), consistent with minimal growth in thick ice areas[53,54]. Estimates of sea ice production using this technique have been found to be consistent within 20 to 25% of in-situ estimates derived by oceanographic measurements[22]. This methodology captures sea ice formation in the Ross Ice Shelf and Terra Nova Bay polynyas and in areas to the north of the Ross Ice Shelf polynya where sea ice is frequently thin and therefore relatively high growth occurs (see Fig. 3). Values are then spatially integrated over the Ross Sea continental shelf (inshore the 1000 m isobath, see Figs. 3a and 3b) and temporally integrated between March and October to obtain yearly sea ice production as shown in Fig. 2 and Extended Data Fig. 3. Coastal polynyas are defined as areas where sea ice production is more than 5 m year^{-1}. As a consequence, the edge of the polynyas changes between years. Sea ice production in polynyas is shown in Extended Data Fig. 3.

Two other complementary methods can be used to infer sea ice formation: 1) a sea ice concentration budget[23] and 2) calculating the net (net = out-in) sea ice area that exits the Ross Sea continental shelf[24-26] (using Kimura and Pathfinder products, see above). These methods reflect the "whole-shelf" sea ice formation and do not capture coastal polynyas (see below for sea ice concentration budget). They both provide evidence of increased sea ice formation between 2015 and 2018 (see Extended Data Figs. 4e and 9). However, we highlight that these methodologies do not account for sea ice thickness and therefore they cannot provide volume changes.

4) *Climate indices*

The leading mode of atmospheric variability in the Southern Hemisphere is described by the Southern Annular Mode (SAM) index. To the first order, variability of SAM is associated with strengthening (positive phase) and weakening (negative phase) of the westerly winds over the entire Southern Hemisphere. Monthly SAM is provided by the British Antarctic Survey[55] (https://legacy.bas.ac.uk/met/gjma/sam.html). Monthly SAM values are standardized before analysis.

The Southern Oscillation Index (SOI) captures variability associated with El Niño and La Niña cycles. We used monthly SOI provided by NCAR (https://climatedataguide.ucar.edu/climate-data/southern-oscillation-indices-signal-noise-and-tahitidarwin-slp-soi). Monthly SOI values are standardized before analysis.

Statistical Analysis

This study focuses on interannual variability and anomalies are defined accordingly. Anomalies for yearly datasets (DSW salinity, cumulative sea ice formation and cumulative sea ice import), are obtained by removing climatological mean and trend calculated over the temporal period covered by the data. The remaining datasets used to estimate summer and winter anomalies (sea ice concentration, winds, mean sea level pressure and climate indices) are first averaged into monthly means, except for climate indices that are already monthly values. Then, monthly anomalies are obtained by subtracting the climatological monthly mean and trend estimated over the temporal period covered by the data. Finally, summer (November to February) and winter (March to October) anomalies are obtained by averaging the monthly anomalies over the corresponding months. Climatologies and trends are calculated over the period 1992 to 2018, except for DSW salinity which is calculated over the period 1994-2018 when data are available.

Anomalies as defined above are then used to calculate the linear correlation (Pearson correlation) between different variables. The correlation between sea ice formation and DSW salinity is calculated at different lags. Autocorrelation is not included in the significance computation (Student *t* test) since the DSW salinity time series has several gaps and the decorrelation time cannot be properly quantified. The decorrelation time for all other time series is effectively zero, since the autocorrelation function falls below 1/e at one year lag in all cases.

We use summer anomalies to perform a multiple linear regression of SAM and SOI onto mean sea level pressure (Fig. 5). To investigate the 2015-2018 period characterized by positive SAM and negative SOI anomalies, we invert SOI values (i.e. from negative to positive and viceversa). In this way, the regression model captures atmospheric variability associated with concurrent positive SAM and negative SOI. In Figs. 5 c and 5d we show the SAM/SOI component based on the coefficients of the multiple regression. Atmospheric anomalies are scaled to better describe the 2015-2018 period (SAM anomaly = 0.5; SOI anomaly = -1 as observed during the 2015-2016 El-Niño). In most of the Ross and Amundsen seas, the p-value is lower than 0.1 (not shown), indicating that the regression well captures the superposition of deepening/rising of the Amundsen Sea Low related to SOI and the falling/rising pressures near the coast during positive/negative SAM. In Fig. 5 we plot winds derived by the mean sea level pressure (i.e. geostrophic winds). The multiple regression performed onto winds (Extended Data Fig. 8) mirrors the geostrophic winds shown in Fig. 5. However, the p-value of the regression onto winds is generally larger than 0.1 near the coast (not shown). This is due to local processes (e.g. katabatic winds), not related to large scale climatic forcing, that "add noise" to the wind variability near the coast. On the other hand, mean sea level pressure and associated geostrophic winds reflect the large scale forcing, which is the focus of this work.

Freshwater sources to the Ross Sea continental shelf

Our analysis shows a strong positive correlation between yearly sea ice formation and DSW salinity (Extended Data Fig. 3), including an increase between 2015 and 2018. Another mechanism that could have driven the recent increase in DSW salinity is reduced freshwater import from the Amundsen Sea. However, while we cannot discount some contribution from freshwater import, we argue that this mechanism is unlikely to be the dominant driver of the recent enhanced DSW salinity for the following reasons. 1) Modelling work[16,56] shows that the response of dense waters over the Ross Sea continental shelf to changes in freshwater import from the Amundsen Sea is not immediate. This because of the time (~3-4 years[56]) required for freshwater injected through a narrow entrance in the eastern Ross Sea to spread all over the continental shelf and thus for dense waters to adjust to this "localized input". In contrast, our observations show rapid and concurrent salinification over the entire continental shelf, with similar rates of salinification observed on the western and eastern Ross Sea continental shelf (Fig. 2a and Extended Data Fig. 2f). 2) Recent (post-2013) hydrographic observations do not show any signal of reduced freshwater inflow into the Ross Sea from the Amundsen Sea[27], as would be needed to explain the observed salinification of dense waters, especially on the eastern shelf close to the source of freshwater. 3) Ice sheet discharge into the Amundsen Sea, which is argued to be the main source of the multi-decadal freshening in the Ross Sea[9], has continued to increase over the past two decades[28,57].

We also note that basal melting of ice shelves in the Amundsen Sea is dominated by decadal variability[58], whose oscillations are expected to be much larger than any long term trend[59]. For example, basal melting in the early 2000s was comparable to that observed in the mid- 2010s, with higher values around 2010[58]. This decadal signal affects the rates of thinning and acceleration of Amundsen Sea ice streams[58-60]. However, none of these ice streams have actually decelerated or thickened appreciably, and basin-wide average results show an overall signal of continued ice shelf thinning and ice stream acceleration throughout the recent period[28,57,60]. This implies that iceberg discharge has increased in recent decades, at least during periods of low basal melting. While the exact location of iceberg melting is unknown, modelling studies[61-63] show that a large fraction of freshwater released by melting of "Amundsen" icebergs occurs within coastal currents that transport freshwater toward the Ross Sea continental shelf. This might explain why decreased freshwater import into the Ross Sea has not been detected in recent years[27] despite the drop in basal melting of ice shelves in the Amundsen Sea[58], and why long-term salinity observations have not detected any decadal signal in the Ross Sea[9]. To conclude, we infer that while freshwater import can influence low frequency (multi-year to decadal) variability of DSW salinity and most likely explains the multi-decadal freshening[9], higher frequency (interannual) variability is dominated by sea ice formation, including the recent salinity increase.

Changes in the intrusions of salty Circumpolar Deep Water onto the continental shelf can also influence properties of shelf waters in the Ross Sea[64]. However, these intrusions are localized in troughs[14] and therefore changes in such intrusions are unlikely to explain synchronous changes in salinity over the entire shelf. Furthermore, model simulations[56] suggest that stronger intrusions, required to increase salinity on the continental shelf, occur when along-shelf break winds strengthen. Stronger winds at the shelf break were not observed between 2015 and 2018 (Extended Data Fig. 1). Other local sources, such as freshwater fluxes from the Ross Ice Shelf or precipitation, are also unlikely to explain the observed DSW salinification, since their contribution to the freshwater budget is much smaller than that due to import from the Amundsen Sea[27].

Sea ice concentration budget

We calculate a budget[23] based on the rate of change in sea ice concentration and associated drivers (i.e. advection, divergence, thermodynamics and mechanical processes). We use satellite-derived sea ice concentration (AMSR-E/AMSR2) and drift (Kimura) to estimate the budget of sea ice concentration *C*:

$$\frac{\partial C}{\partial t} = -\boldsymbol{u} \cdot \nabla C - C\nabla \cdot \boldsymbol{u} + residual$$

where $\boldsymbol{u}$ is the sea ice velocity vector (m s^{-1}). The term on the left hand side represents the rate of change of sea ice concentration, or sea ice intensification. The first term on the right hand side relates sea ice intensification to sea ice advection, while the second term is associated with sea ice divergence. The residual term includes thermodynamics (sea ice melting and freezing) and mechanical redistribution (ridging and rafting of sea ice, or simply "ridging"). Positive values of the residual term are associated with net sea ice growth, while negative values are associated with sea ice melting or ridging. During the winter, sea ice melting is low and therefore negative values of the residual are mostly associated with net ridging. During summer, when sea ice concentration decreases, negative values are linked with net melting. We note that the budget is associated with changes in sea ice area and not volume, since observations of Antarctic sea ice thickness are limited[65]. For this reason this budget cannot be used to estimate the total sea ice formation or melting, but only the changes in sea ice area associated with these processes.

Extended Data Fig. 9 shows maps of the divergence and residual term during winter. The resolution of the dataset (60-km grid plus the differentiation required for the budget calculation) do not allow any representation of polynyas near the coast. Therefore, this budget has to be interpreted in terms of "large-scale" features of the southern Ross Sea. On the south-western continental shelf, the budget shows strong divergence and sea ice formation, consistent with high sea ice formation in the Ross Ice Shelf and Terra Nova Bay polynyas. To the north and east of this area, sea ice convergence and ridging occur, especially near Cape Adare. Between 2015 and 2018, negative anomalies of divergence and positive anomalies of the residual term can be observed. This indicates more sea ice formation (and more divergence) on the south-western continental shelf, and less ridging (and less convergence) to the north and east. These results confirm enhanced sea ice formation concurrent with increased divergence and reduced ridging between 2015 and 2018 on the Ross Sea continental shelf.

Extended Data Fig. 6c shows the summer cumulative (in time) residual term of the sea ice budget spatially integrated over the Ross Sea continental shelf. Only negative values are included in the calculation to provide a proxy for the amount of sea ice area lost due to sea ice melting. No signal of anomalous sea ice melting can be detected between 2015 and 2018. We note that the same calculation performed including only times when sea ice concentration was less than 90% (i.e. when no ridging is expected) provides analogous results (not shown). Moreover, there were neither anomalous strong southerly winds (Extended Data Fig. 6a) nor elevated surface air temperature between 2015 and 2018 (Extended Data Fig. 6b), confirming that reduced sea ice concentration in summer over the southern Ross Sea was driven by reduced sea ice import from the Amundsen Sea.

The sea ice budget just introduced provides an important tool to investigate sea ice processes and their temporal changes. However, satellite data required to perform this budget cover only a relatively short and discontinous period (2003-2010 and 2013-2018). Therefore, while this budget is useful as a consistency check for our analysis and provides an independent confirmation of the increased sea ice formation between 2015 and 2018 over the Ross Sea continental shelf, it currently cannot be used alone to investigate temporal variability in sea ice dynamical and thermodynamical processes for periods longer than a few years.

Data availability

Oceanographic data were collected and made publicly available by the International Global Ship-based Hydrographic Investigations Program (GO-SHIP; http://www.go-ship.org/), by the National and Oceanic and Atmospheric Administration NOAA (https://www.nodc.noaa.gov), by the International Argo Program and the national programs that contribute to it (http://www.argodatamgt.org; http://www.argo.ucsd.edu; http://argo.jcommops.org), by the Italian National Antarctic Research Programme (PNRA; http://morsea.uniparthenope.it), and during Nathaniel B. Palmer expeditions in 2013 and 2018 as part of the TRACERS (https://doi.org/10.1594/IEDA/320068) and CICLOPS (https://www.bco-dmo.org/dataset/783911).

Atmospheric data are provided by the ECMWF ERA5 re-analysis (https://www.ecmwf.int/en/forecasts/datasets/reanalysis-datasets/era5). The National Snow and Ice Data Center provides the satellite-derived data used in this study: sea ice concentration and brightness temperature (https://nsidc.org/data/G02202/versions/3; https://nsidc.org/data/AU_SI12/versions/1; https://nsidc.org/data/smmr_ssmi), sea ice motion (https://nsidc.org/data/NSIDC-0116/versions/4).

Climate indices are provided by the British Antarctic Survey (Southern Annular Mode: https://legacy.bas.ac.uk/met/gjma/sam.html) and by the National Centre for Atmospheric Research (Southern Oscillation Index: https://climatedataguide.ucar.edu/climate-data/southern-oscillation-indices-signal-noise-and-tahitidarwin-slp-soi).

Code availability

Matlab scripts used for the analyses described in this study can be obtained from the corresponding author on reasonable request.

References

43. Boyer, T. P. et al. World Ocean Database 2013, NOAA Atlas NESDIS 72 (eds Levitus, S & Mishonov, A.) 209 (Silver Spring, MD) http://doi.org/10.7289/V5NZ85MT (2013).
44. Johnson, G. C. & Orsi, A. H. (1997). Southwest Pacific Ocean water-mass changes between 1968/69 and 1990/91. *J. Clim.* **10**(2), 306–316 (1997).
45. Roemmich, D. *et al.* Deep SOLO: A full-depth profiling float for the Argo Program. *J. Atmos. Oceanic Technol.* **36**, 1967–1981 (2019).
46. McDougall, T. J. & Barker, P. M. Getting Started with TEOS-10 and the Gibbs Seawater (GSW) Oceanographic Toolbox (SCOR/IAPSO WG127, ISBN 978-0-646-55621-5, 2011), 28 pp. (2011).

47. Hersbach, H. & Dee, D. ERA5 reanalysis is in production. ECMWF Newsletter, No. 147, ECMWF, Reading, United Kingdom, 7 (2016).
48. Meier, W. N., *et al*. *NOAA/NSIDC Climate Data Record of Passive Microwave Sea Ice Concentration, Version 3* (National Snow and Ice Data Center, 2017).
49. Meier, W. N., Markus, T. & Comiso, J. C. 2018. *AMSR-E/AMSR2 Unified L3 Daily 12.5 km Brightness Temperatures, Sea Ice Concentration, Motion & Snow Depth Polar Grids, Version* (National Snow and Ice Data Center, 2018).
50. Tschudi, M., Meier, W. N., Stewart, J. S., Fowler, C. & Maslanik, J. *Polar Pathfinder Daily 25 km EASE-Grid Sea Ice Motion Vectors, Version 4* (National Snow and Ice Data Center, 2019).
51. Kimura, N. Sea ice motion in response to surface wind and ocean current in the Southern Ocean. *J. Meteorol. Soc. Jpn* **82**, 1223–1231 (2004).
52. Kwok, R. Ross Sea ice motion, area flux, and deformation. *J. Clim.* **18**, 3759–3776 (2005).
53. Lytle, V. I. & Ackley, S. F. Heat flux through sea ice in the western Weddell Sea: Convective and conductive processes. *J. Geophys. Res.* **101**, 8853–8868 (1996).
54. Lytle, V. I. *et al*. Ice formation in the Mertz Glacier polynya, East Antarctica, during winter. *Ann. Glaciol.*, **33**, 368–372 (2001).
55. Marshall, G. J. Trends in the Southern Annular Mode from observations and reanalyses. *J. Clim.* **16**, 4134–4143 (2003).
56. Dinniman, M. S., Klinck, J. M., Hofmann, E. E. & Smith, W. O. Effects of projected changes in wind, atmospheric temperature, and freshwater inflow on the Ross Sea. *J. Clim.* **31**, 1619–1635 (2018).
57. Shepherd, A. et al. Mass balance of the Antarctic ice sheet from 1992 to 2017. *Nature* **556**, 219–222 (2018).
58. Jenkins, A. et al. West Antarctic Ice Sheet retreat in the Amundsen Sea driven by decadal oceanic variability. *Nat. Geosci.* **11**, 733–738 (2018).
59. Holland, P.R., *et al.* West Antarctic ice loss influenced by internal climate variability and anthropogenic forcing. *Nat. Geosci.* **12,** 718–724 (2019).
60. Paolo, F. S. et al. Response of Pacific-sector Antarctic ice shelves to the El Niño/Southern Oscillation. *Nat. Geosci.* **11**, 121–126 (2018).
61. Stern, A. A., Adcroft, A. & Sergienko, O. The effects of Antarctic iceberg calving-size distribution in a global climate model. *J. Geophys. Res. Oceans* **121**, 5773–5788 (2016).
62. Merino, N., *et al.* J. Antarctic icebergs melt over the Southern Ocean: Climatology and impact on sea ice. *Ocean Model.* **104**, 99–110 (2016).

63. Rackow, T., *et al.* Simulation of small to giant Antarctic iceberg evolution: Differential impact on climatology estimates. *J. Geophys. Res. Oceans* **122**, 3170–3190 (2017).
64. Castagno, P., Falco, P., Dinniman, M. S., Spezie, G. & Budillon, G. Temporal variability of the Circumpolar Deep Water inflow onto the Ross Sea continental shelf. *J. Mar. Syst*. **166**, 37–49 (2017).
65. Worby, A. P. *et al.* Thickness distribution of Antarctic sea ice. *J. Geophys. Res.* **113,** C05S92 (2008).

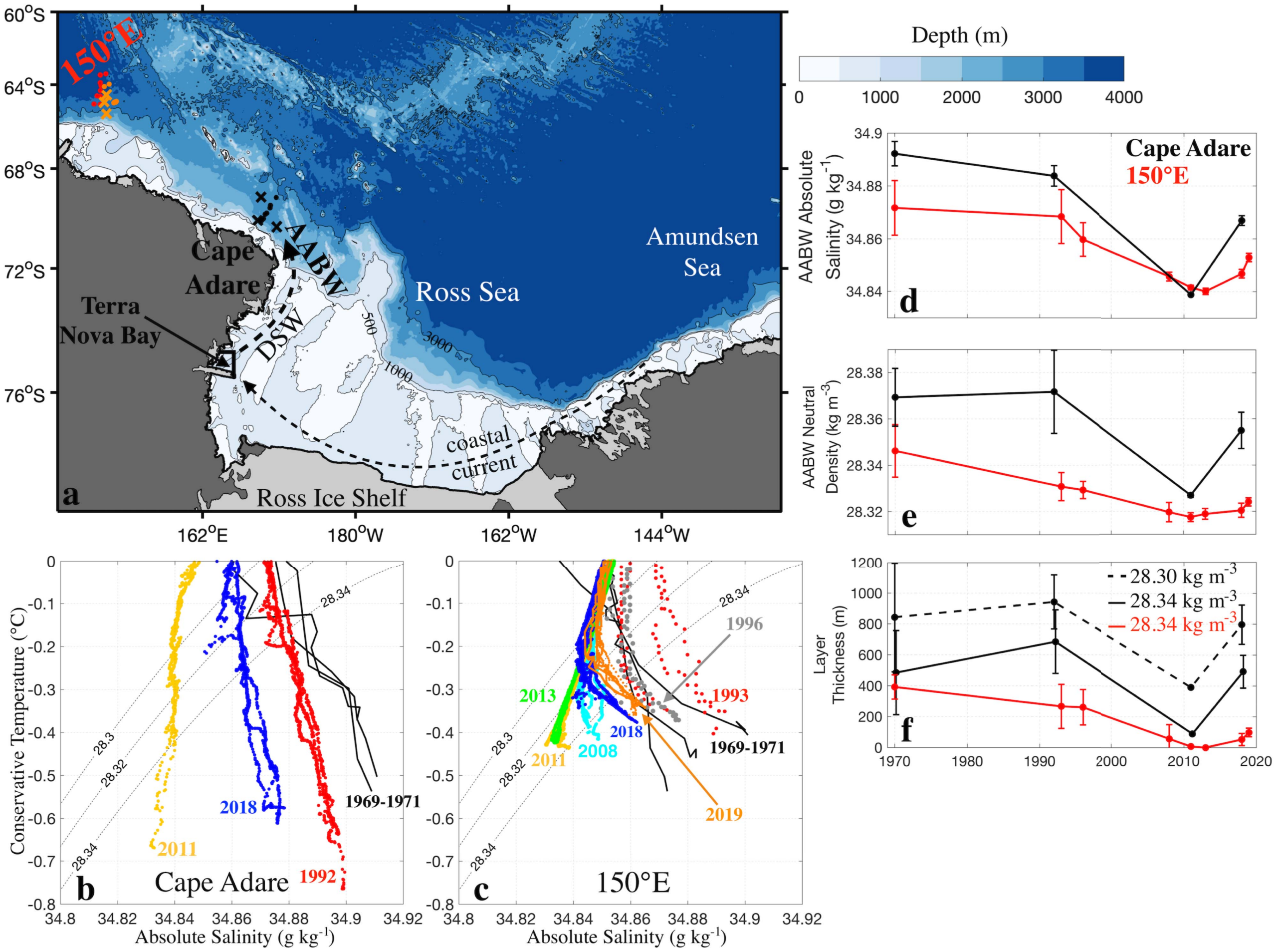

Fig. 1| Recovery of AABW formed in the Ross Sea. a, Map of the study area with bathymetry overlaid. Crosses indicate observations from the Eltanin expedition in 1969-1971, while orange dots denote data collected by a deep float in 2019 (see Methods). **b**, **c**, Conservative temperature (°C) versus absolute salinity (g kg^{-1}) at Cape Adare and at 150°E (see location in **a**). Overlaid are the 28.30, 28.32 and 28.34 kg m^{-3} neutral density surfaces for reference. **d**, **e**, Average AABW absolute salinity and neutral density. AABW is defined as water denser than 28.30 kg m^{-3}. **f**, Thickness of the 28.30 (dashed black) and 28.34 (solid black) kg m^{-3} layers at Cape Adare and thickness of the 28.34 kg m^{-3} layer at 150°E (red). Thickness is calculated between the depth of the density surface and the sea floor. Mean (dots) and standard deviation (vertical bars) are calculated using observations collected each year along the two transects. Observations from the Eltanin expedition are temporally averaged between 1969 and 1971.

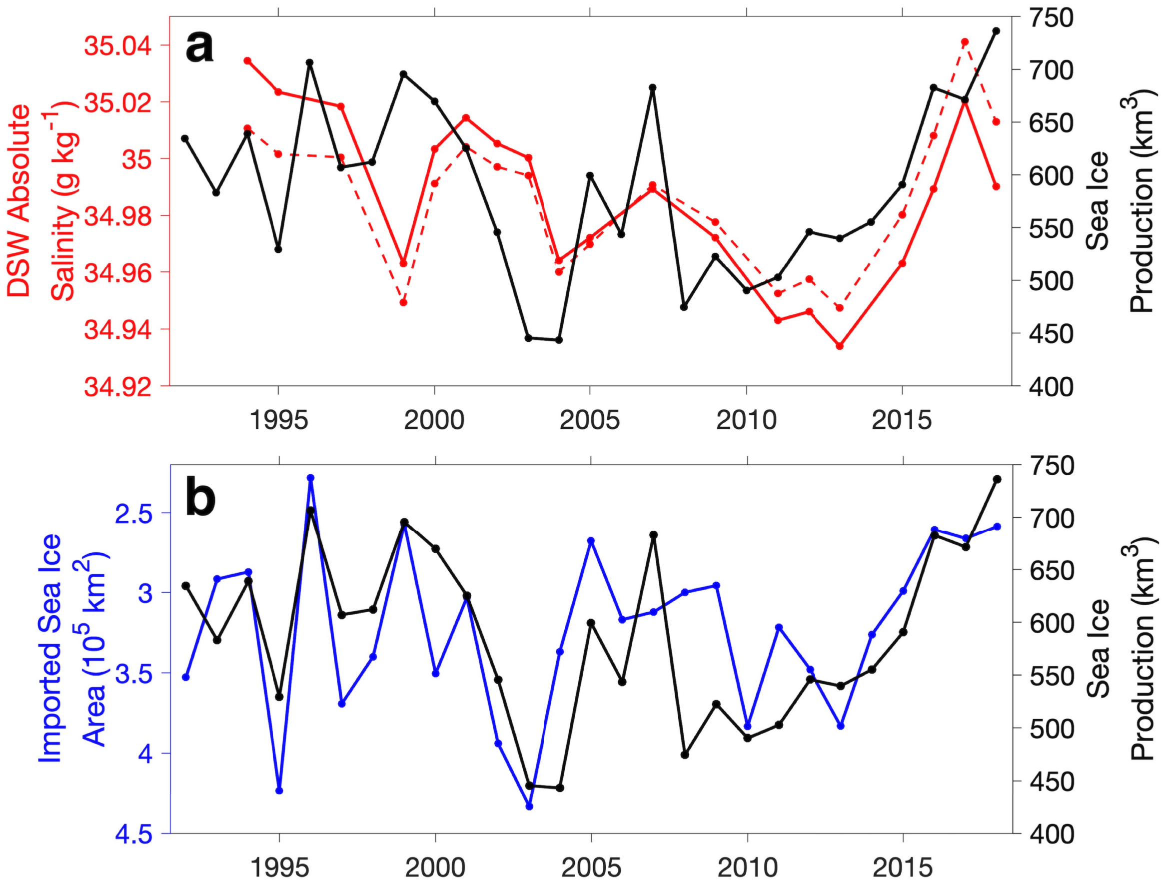

Fig. 2| Link between DSW salinity, sea ice production and import. a, DSW salinity (g kg^{-1}), solid red) measured near the sea floor in Terra Nova Bay (see Methods) and yearly (March to October) sea ice production (km^3, solid black) over the Ross Sea continental shelf between 1992 and 2018. Note that some years are missing in the DSW salinity time series. The dashed red line is the detrended DSW salinity. **b**, Yearly (November to October) sea ice area (10^5 km^2) imported from the Amundsen Sea into the Ross Sea (blue), calculated across the gate shown in Fig. 4c (see Methods). Note that the y-axis is reversed. Overlaid is the yearly sea ice production as in **a**.

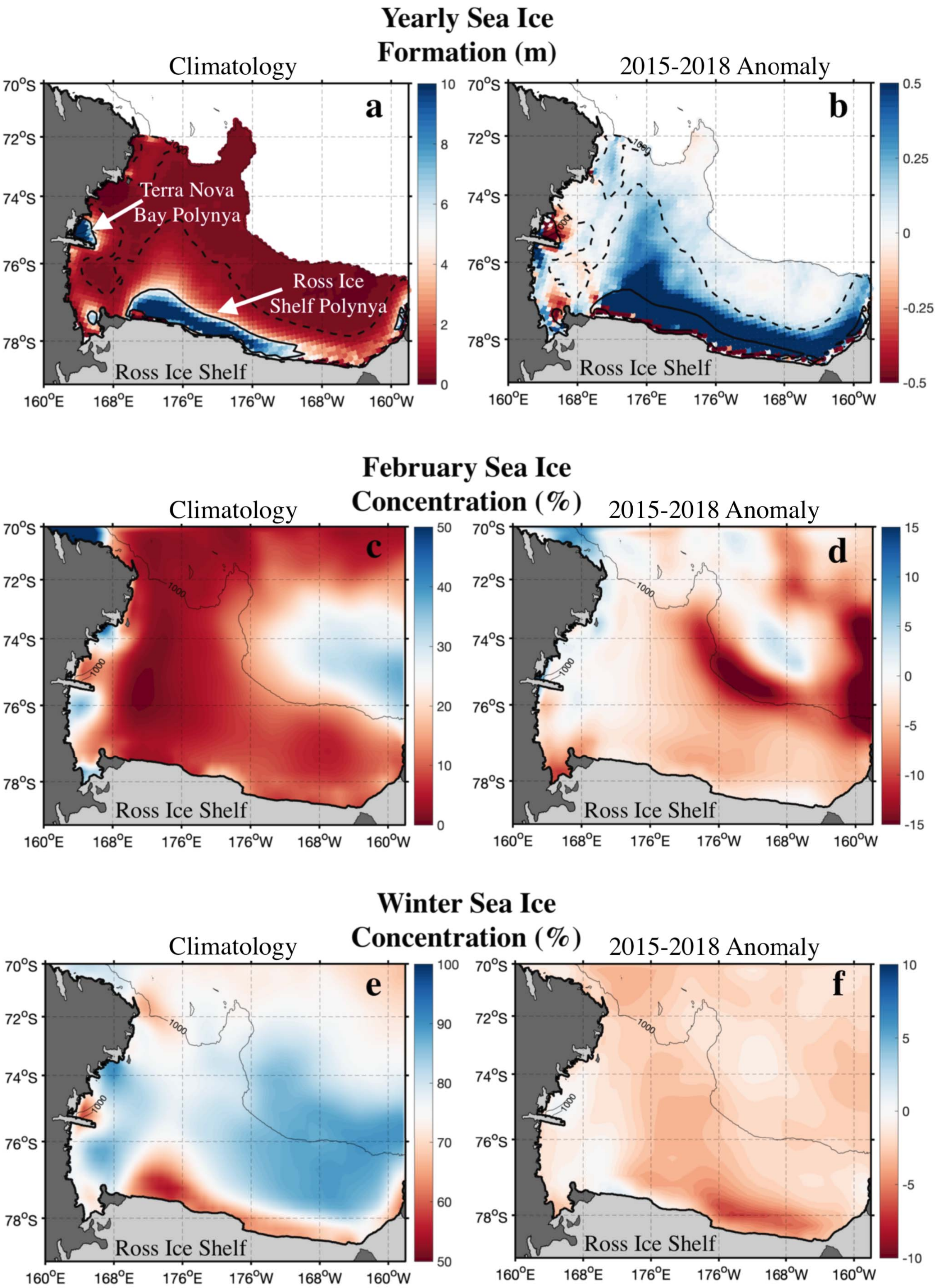

Fig. 3| Sea ice changes in the Ross Sea. a, Climatological yearly (March to October) sea ice production (m) over the Ross Sea continental shelf. **b**, Anomaly of sea ice production temporally averaged between 2015 and 2018. In **a** and **b** the 5-m yearly sea ice production contour is in solid black to capture the edge of coastal polynyas, while the 0.5-m contour in dashed black highlights areas outside coastal polynyas with relatively high rates of sea ice production. **c**, Climatological sea ice concentration (%) in February over the southern Ross Sea. **d**, Anomaly of February sea ice concentration temporally averaged between 2015 and 2018. **e**, **f** Same as **c**, **d** but for winter (March to October). Climatologies and anomalies are defined in the Methods.

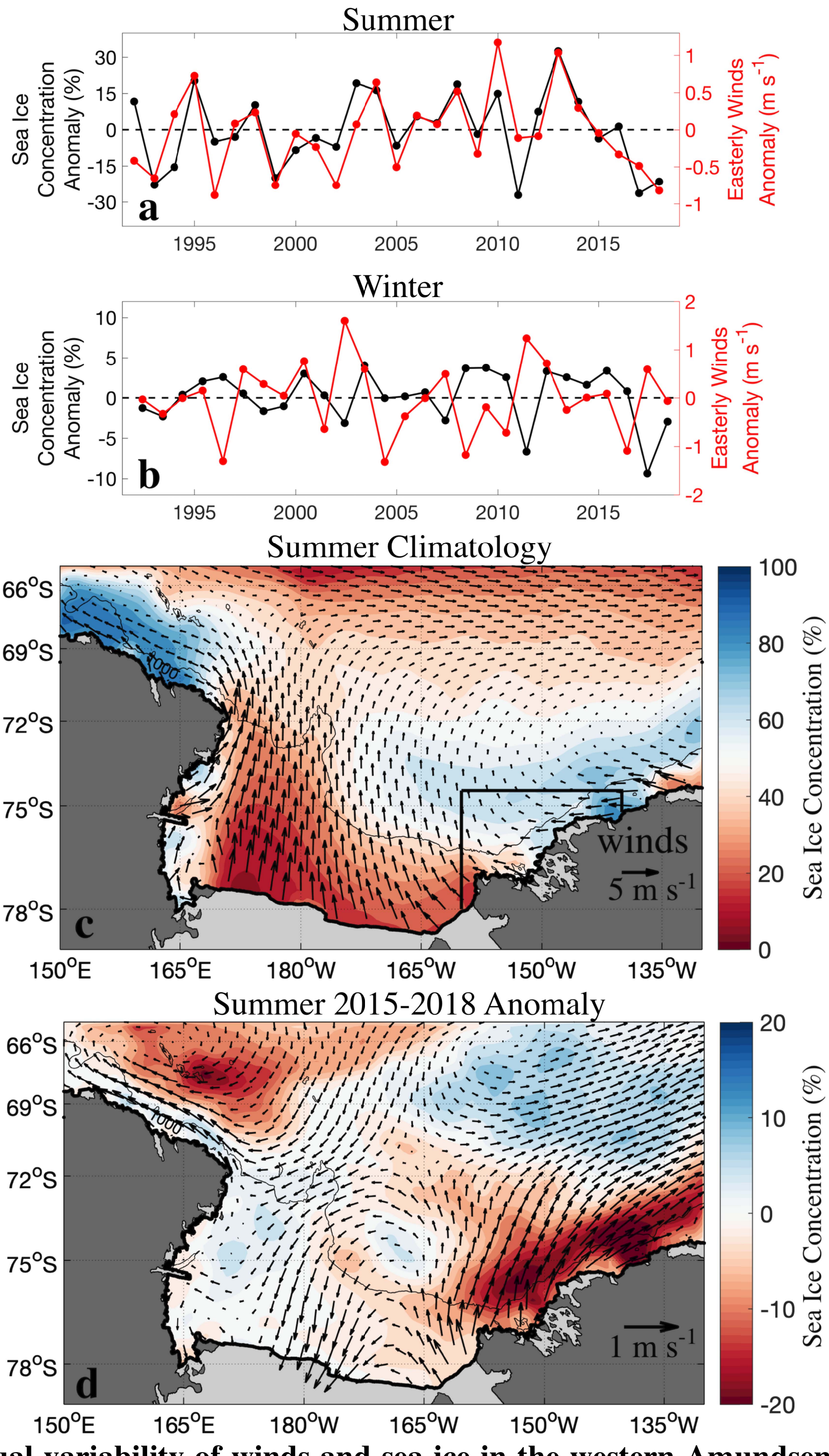

Fig. 4| Interannual variability of winds and sea ice in the western Amundsen Sea. a, Summer (November to February) anomalies of easterly winds (m s⁻¹) and sea ice concentration (%) in the western Amundsen Sea between 1992 and 2018 (see Methods). Values are obtained from a spatial average inside the black box in **c**. The south-north transect on the western side of the box represents the gate used to estimate the sea ice inflow from the Amundsen to the Ross Sea. Easterly winds are obtained by rotating the coordinate system counterclockwise by 30° to follow the coastline. **b**, Same as **a** for winter (March to October). **c** (**d**) Summer climatology (2015-2018 anomaly) of winds (vectors) and sea ice concentration (background color) in the Ross and western Amundsen seas.

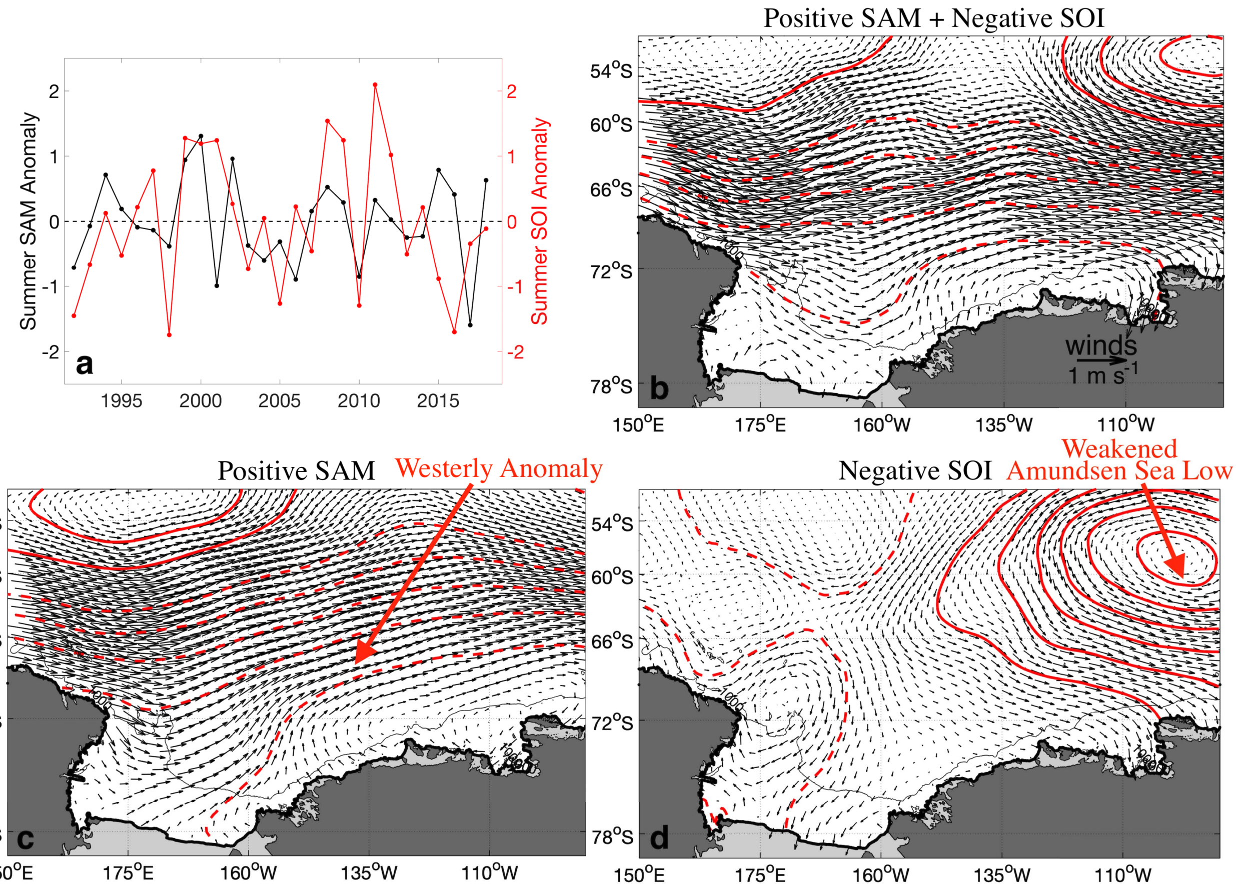

Fig. 5| Anomalous climate forcing between 2015 and 2018. a, Summer anomalies of SAM (black) and SOI (red) between 1992 and 2018. The 2015-2018 period is characterized by positive SAM and negative SOI. **b**, Multiple regression (see Methods) of SAM and SOI onto mean sea level pressure (mbar, red lines), and associated winds (m s⁻¹, black vectors). Contours of mean sea level pressure are every 0.5 mbar. Solid (dashed) lines mean positive (negative) anomalies. **c**, SAM component of the regression. This panel highlights atmospheric variability associated with positive SAM. **d**, Same as **c**, for (negative) SOI. In this panel contours are every 0.25 mbar. Note how both positive SAM and negative SOI cause westerly anomalies over the Amundsen Sea.

?

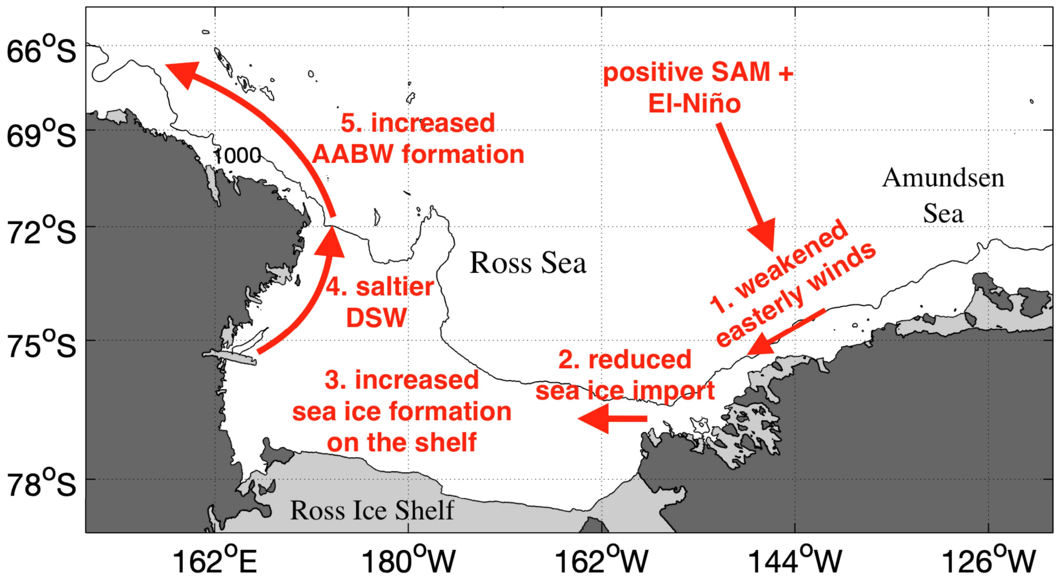

Fig 6| Schematic illustrating the physical mechanisms driving enhanced AABW formation in the Ross Sea. The unusual combination of positive SAM and El-Niño resulted in weaker easterly winds in the western Amunsen Sea, less import of sea ice, and a more open sea ice pack with higher rates of sea ice formation on the Ross Sea continental shelf. The resulting increase in DSW salinity enhanced the formation of AABW.

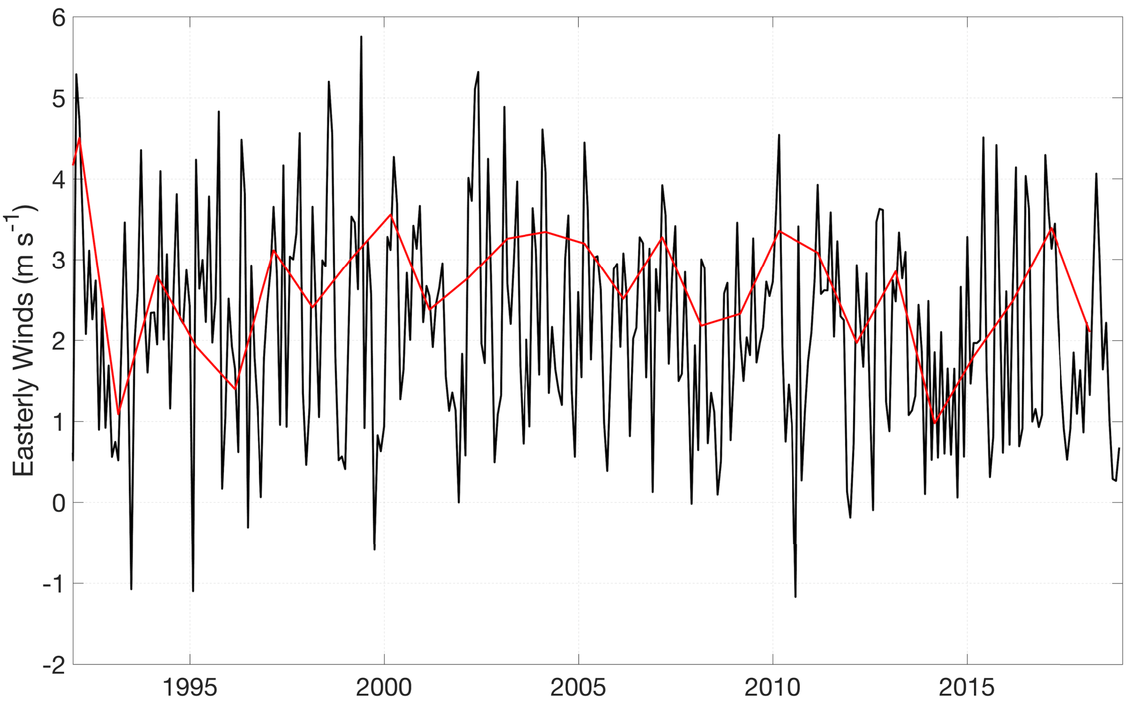

Extended data Fig. 1. **Easterly winds at the shelf break of the western Ross Sea**. Following Gordon et al.[?], winds are obtained by rotating the coordinate system clockwise by 40° to follow shelf break isobaths and are spatially averaged in the box 70S°-75°S, 175°E-175°W. Monthly data are in black while data temporally averaged between February and April are in red. The "Feb-Apr winds" are shown because the strongest wind-driven export of DSW from the western Ross Sea continental shelf occurs in these months[?].

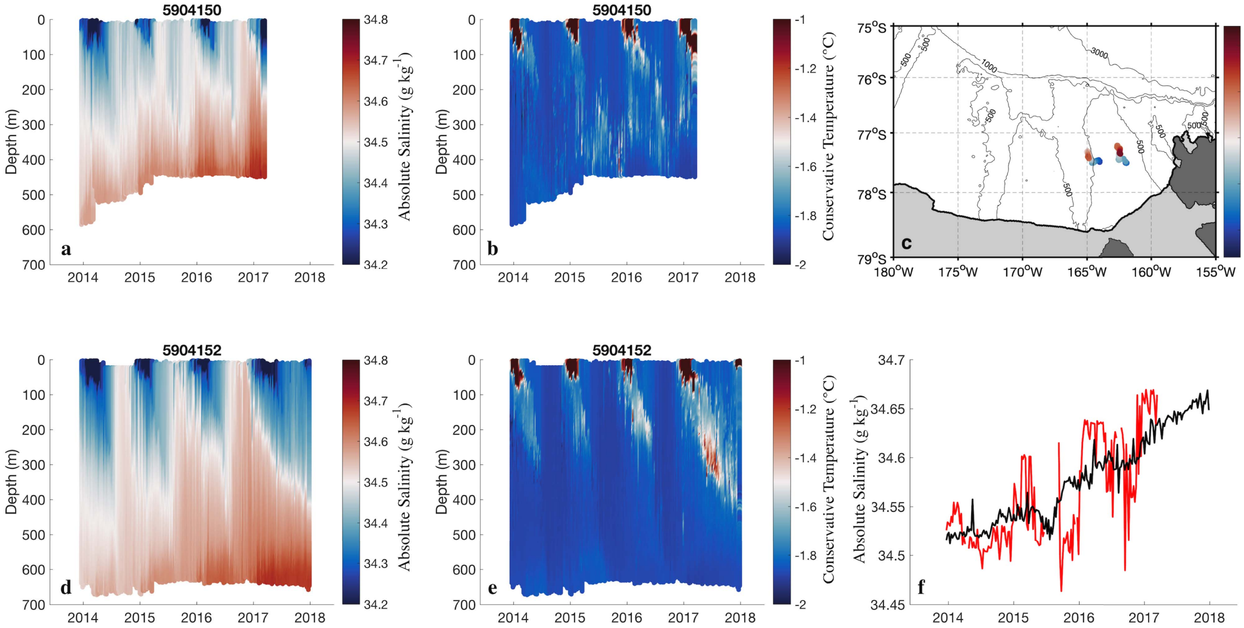

Extended Data Fig. 2. **Salinification of dense waters on the eastern Ross Sea continental shelf.** **a**, Time series of absolute salinity (g kg^{-1}) collected by a profiling float (WMO: 5904150) between late 2013 and early 2017 (map in **c**). **b**, same as **a** for conservative temperature (°C). **d**, **e** same **a**, **b** for another profiling float (WMO: 5904152) between late 2013 and early 2018. **f**, Time series of salinity averaged in the bottom 200 m of the water column for water cooler than -1.85°C for float 5904150 (red) and 5904152 (black).

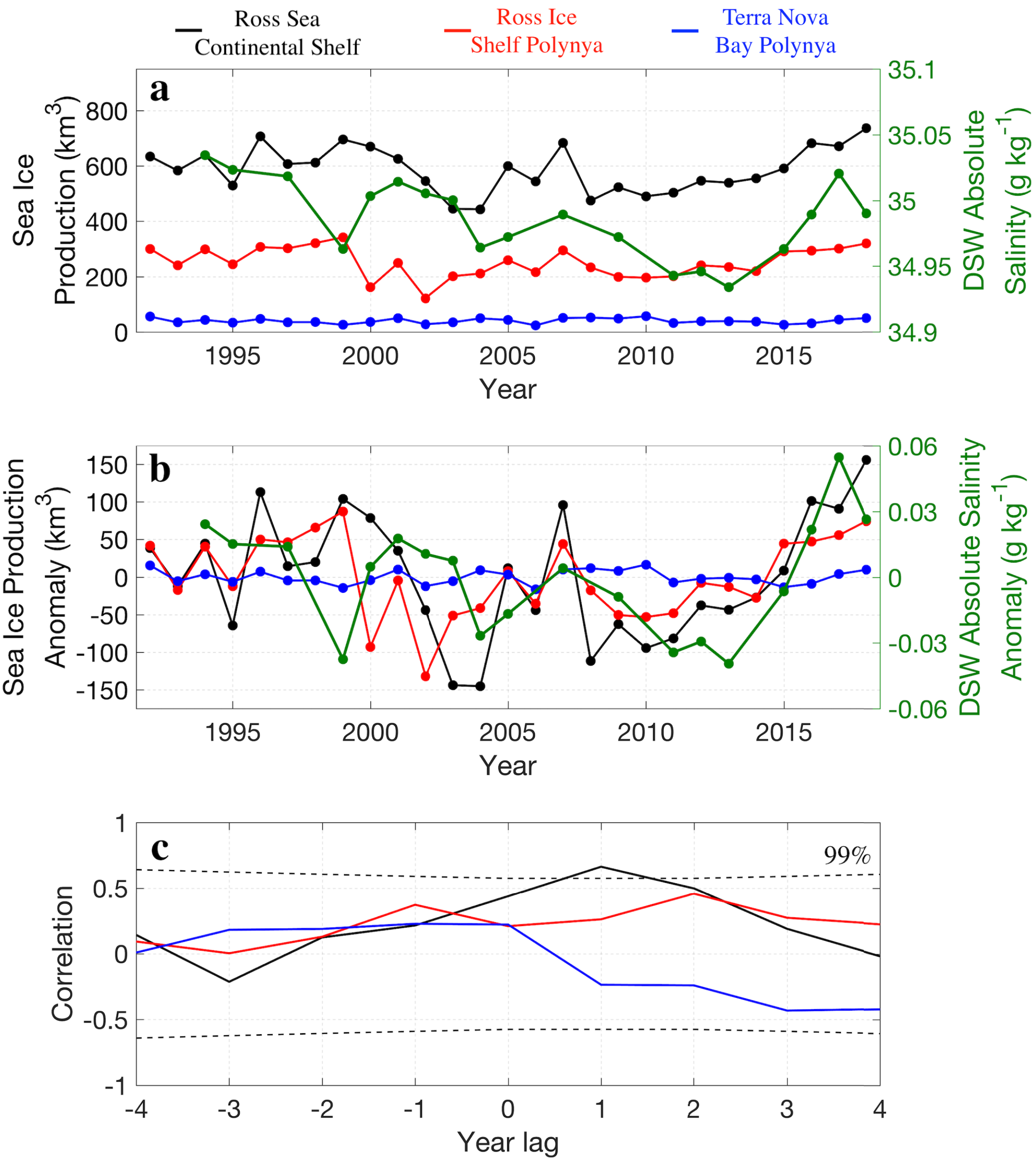

Extended Data Fig. 3. **Link between DSW salinity and sea ice production. a**, Yearly sea ice formation (km) over the entire Ross Sea continental shelf (solid black), Ross Ice Shelf (red) and Terra Nova Bay (blue) polynyas. Polynyas are defined as areas where yearly sea ice formation is larger than 5 m (see Fig. 2). Solid green is DSW absolute salinity (g kg) in Terra Nova Bay. **b**, Same as **a** for anomalies. **c**, Correlation between DSW salinity and yearly sea ice formation (colors the same as **a**, dashed black line represents the 99% confidence interval). Sea ice production leads DSW salinity.

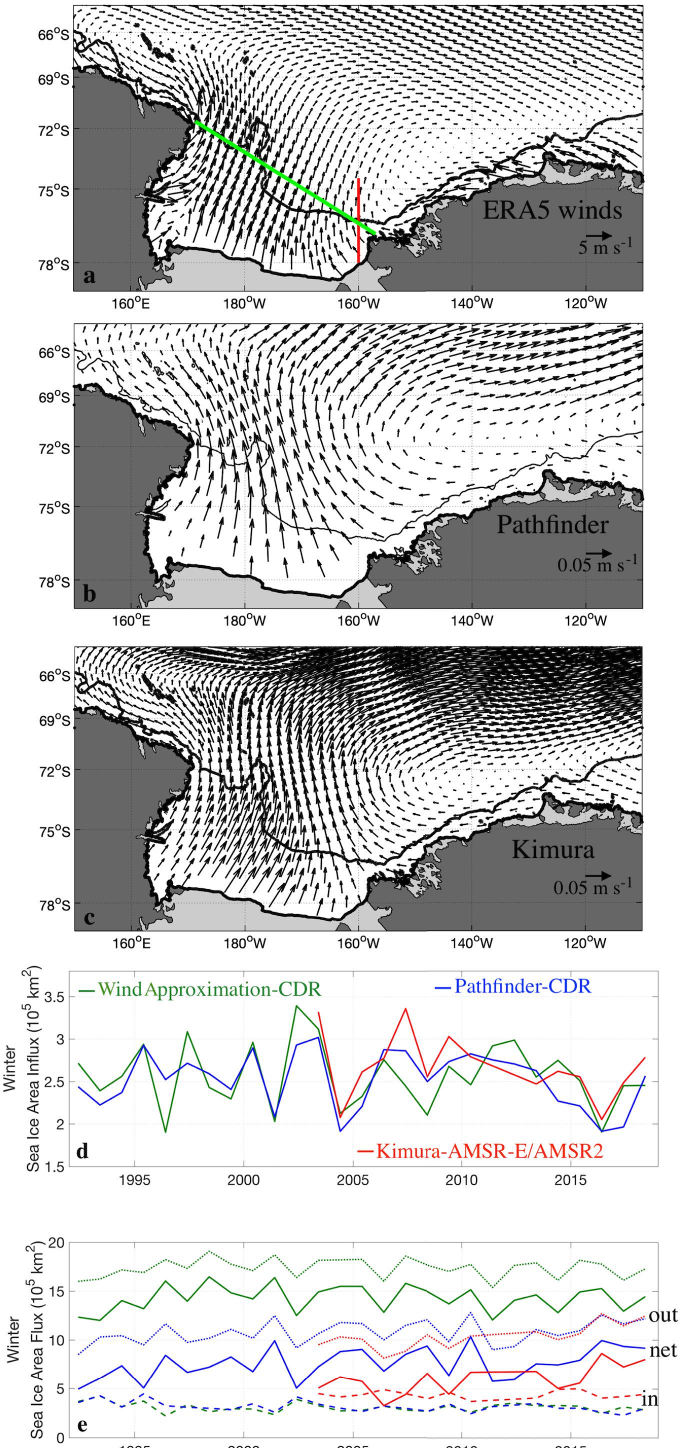

Extended Data Fig. 4. **Sea ice motion and fluxes.** Winter climatology of **a**, winds (m s^{-1}) from ERA5, **b,** sea ice motion (m s^{-1}) from Pathfinder and **c**, sea ice motion from the Kimura dataset. **d**, Winter sea ice area inflow (10^5 km^2) into the southern Ross Sea through the meridional transect shown in red in **a**. Estimates are obtained using the wind-approximation for sea ice motion and CDR for sea ice concentration (green), Pathfinder for sea ice motion and CDR for sea ice concentration (blue), and the Kimura dataset for sea ice motion and AMSR-E/AMSR2 for sea ice concentration (red). The three estimates agree reasonably well with each other. **e**, Winter sea ice area flux through a transect that encloses the Ross Sea continental shelf (green line in **a**). The dashed (dotted) lines indicate sea ice flowing into (out of) the Ross Sea continental shelf. The net (solid) is a proxy for how much sea ice forms on the continental shelf. Note how the wind approximation fails in representing the export, but it well captures the inflow.

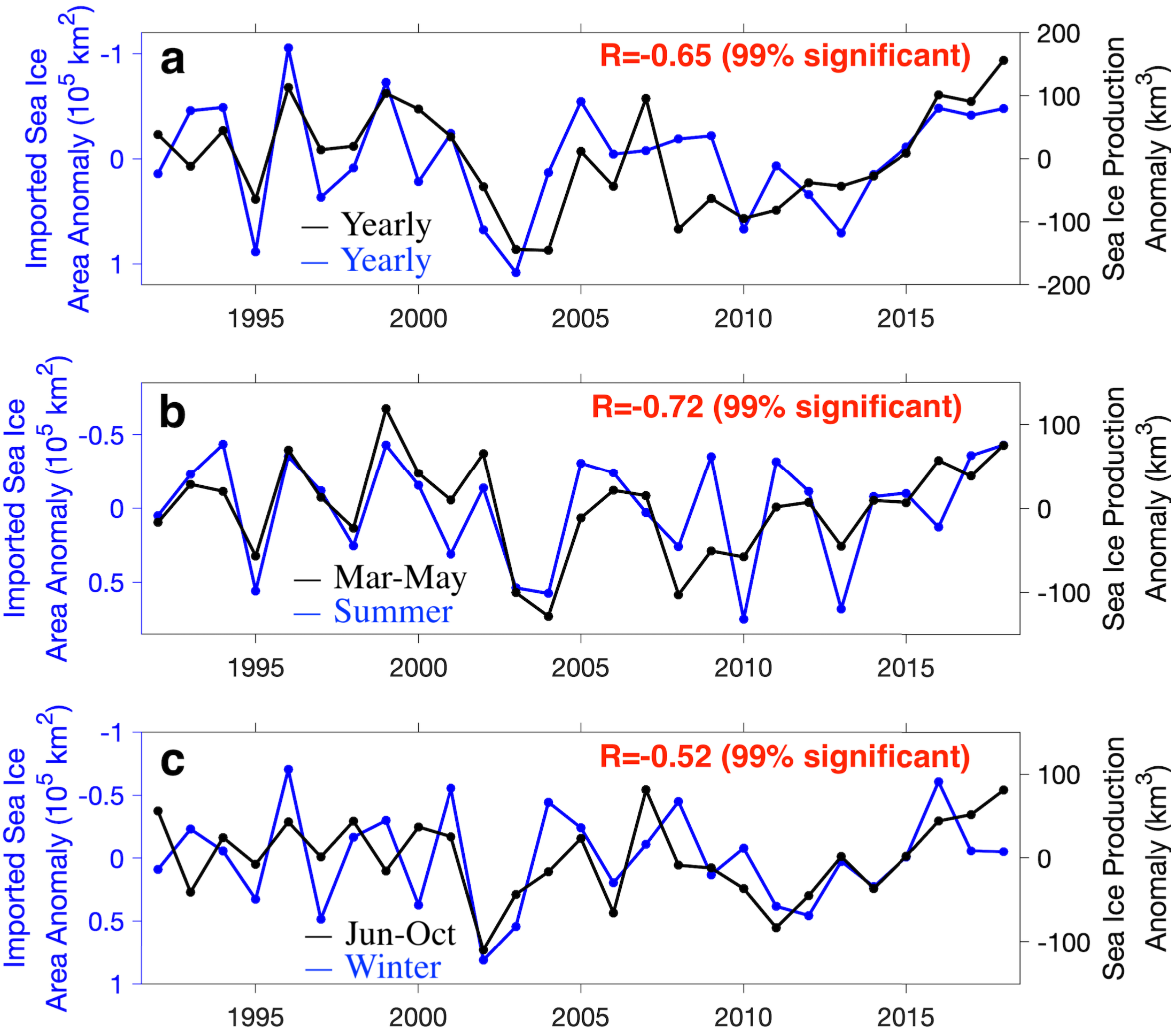

Extended Data Fig. 5. **Link between sea ice formation and import. a**, In blue is the yearly (November to October) anomaly of sea ice area (10⍰ km⍰) imported from the Amundsen Sea into the Ross Sea between 1992 and 2018, calculated across the gate shown in red in Extended Data Fig. 4a. Note that the y-axis is reversed. Overlaid in black is the yearly (March to October) anomaly of sea ice production (km⍰) over the Ross Sea continental shelf (as shown in Extended Data Fig. 3b). **b**, Summer (November to February) anomaly of imported sea ice area and early winter (March to May) sea ice production anomaly. **c**, Winter (March to October) anomaly of imported sea ice area and sea ice production anomaly in late winter (June to October). Correlations between time series shown in each panel are in red.

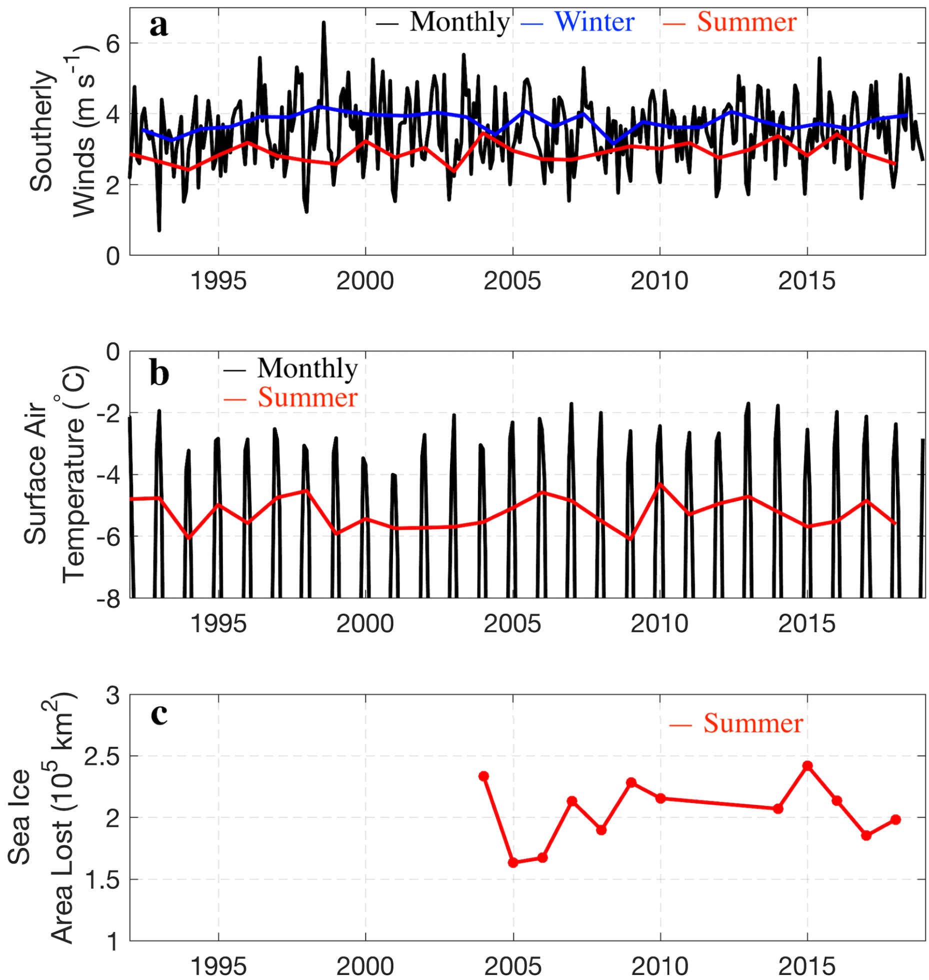

Extended Data Fig. 6. **Ross Sea continental shelf spatial averages. a**, Southerly winds (m s⁇). Monthly data are in black, while values temporally averaged over summer and winter months are in red and blue, respectively. **b**, Surface air temperature (°C). Black and red lines as in **a**. **c**, Sea ice area (10⁇ km⁇) lost on the Ross Sea continental shelf due to sea ice melting (see sea ice concentration budget in the Methods). The values are obtained from the time integration of the residual term between November and February, further integrated over the continental shelf. Only negative values (which in summer is mostly due to melting) are included in the calculation.

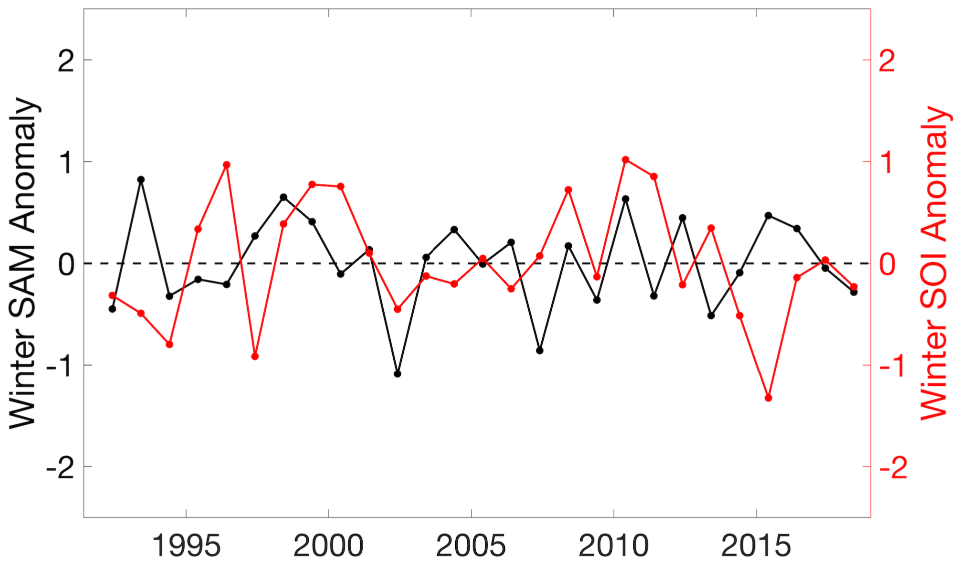

Extended Data Fig. 7. **Winter climate indices.** Anomalies of SAM (black) and SOI (red) during winter.

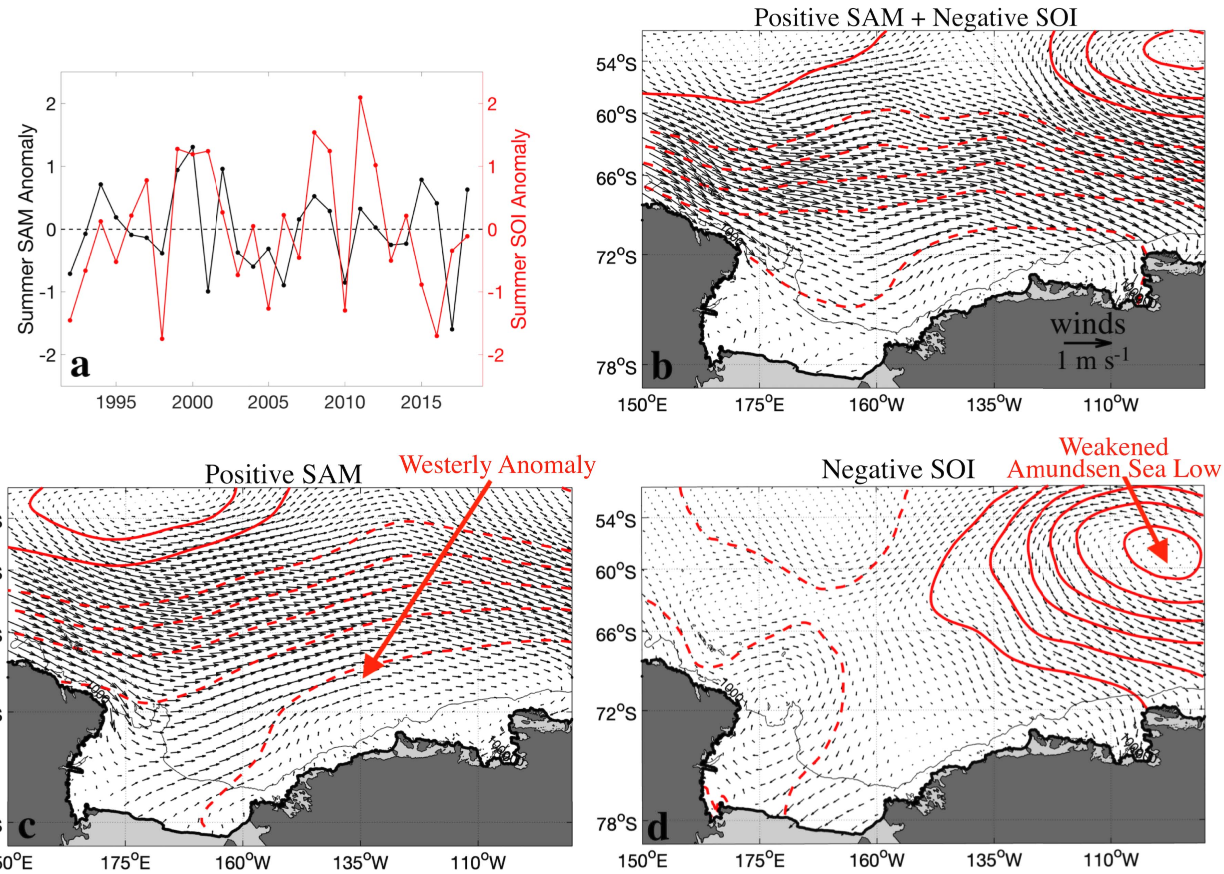

Extended Data Fig. 8. Wind multiple regression analysis. As Fig. 5 but including the multiple regression of SOI and SAM onto winds, instead of showing geostrophic winds derived by the mean sea level pressure.

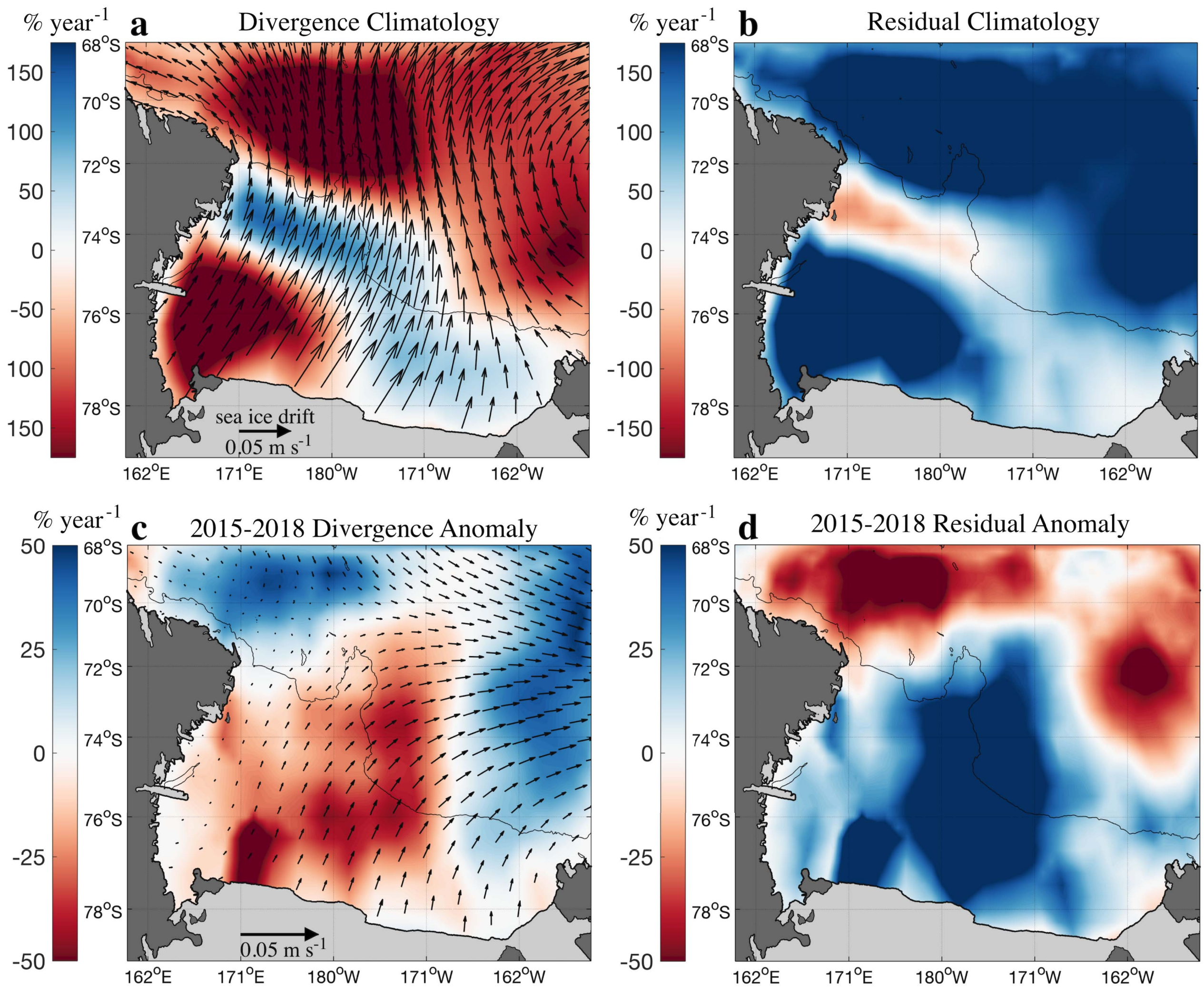

Extended Data Fig. 9. **Sea ice concentration budget. a** (**b**) Winter climatology of the divergence (residual) term of the sea ice concentration budget (see Methods). Values indicate sea ice concentration change over the winter season associated with divergence/residual term. Positive values indicate a source of sea ice (i.e. more divergence is negative, while more sea ice formation is positive). **c** (**d**) Anomalies of the divergence (residual) term temporally averaged between 2015 and 2018. Climatologies are calculated using all available years (i.e. 2003-2010 and 2013-2018). Here anomalies are the deviations from the climatologies. Overlaid in **a** (**c**) are vectors representing the winter climatology (2015-2018 anomaly) of sea ice drift ("Kimura")).